Remote Sensing of Environment 280 (2022) 113209

Contents lists available at ScienceDirect

Remote Sensing of Environment

journal homepage: www.elsevier.com/locate/rse

TROPOMI SIF reveals large uncertainty in estimating the end of plant growing season from vegetation indices data in the Tibetan Plateau

Jilin Yang [a], Xiangming Xiao [b,*], Russell Doughty [b], Miaomiao Zhao [c,d], Yao Zhang [e], Philipp Köhler [f], Xiaocui Wu [g], Christian Frankenberg [f,h], Jinwei Dong [a,*]

[a] Key Laboratory of Land Surface Pattern and Simulation, Institute of Geographic Sciences and Natural Resources Research, Chinese Academy of Sciences, Beijing 100101, China
[b] Department of Microbiology and Plant Biology, Center for Earth Observation and Modeling, University of Oklahoma, Norman, OK 73019, USA
[c] Information Center of Ministry of Ecology and Environment, Beijing 100029, China
[d] State Key Laboratory of Resources and Environment Information System, Institute of Geographic Sciences and Natural Resources Research, Chinese Academy of Sciences, Beijing 100101, China
[e] Sino-French Institute for Earth System Science, College of Urban and Environmental Sciences, Peking University, Beijing 100101, China
[f] Division of Geological and Planetary Sciences, California Institute of Technology, Pasadena, CA 91226, USA
[g] Agroecosystem Sustainability Center, Institute for Sustainability, Energy, and Environment, University of Illinois Urbana-Champaign, Urbana, IL 61801, USA
[h] Jet Propulsion Laboratory, California Institute of Technology, Pasadena, CA 91109, USA

ARTICLE INFO

Edited by Jing M. Chen

Keywords:
Phenology
Photosynthesis
Gross primary production
Solar-induced chlorophyll fluorescence
TROPOMI
Vegetation indices
Tibetan plateau

ABSTRACT

Large-scale land surface phenology (LSP) information has been developed from remote sensing-based vegetation indices (VIs) data. However, there are considerable discrepancies and uncertainties in the LSP data products for the start and end of growing seasons (SOS; EOS) as different vegetation indices and algorithms are used. Here, we used the TROPOspheric Monitoring Instrument (TROPOMI) solar-induced chlorophyll fluorescence (SIF) data to estimate SOS and EOS in the Tibetan Plateau, a global hotspot of vegetation response to climate change. We compared SIF-based phenological metrics to those derived from VIs (e.g., normalized difference vegetation index (NDVI), enhanced vegetation index (EVI), and near-infrared reflectance of vegetation (NIRv)), and gross primary production (GPP) simulated by the vegetation photosynthesis model (VPM). We found relatively small discrepancies in SOS between SIF and VIs, but large differences in EOS. Thus, the length of the growing season derived from VIs was as much as two months longer than that estimated by SIF. These results were consistent across three products, bidirectional reflectance distribution function (BRDF) adjusted (MCD43), standard MODIS (MOD09), and TROPOMI products. The EOS discrepancy remained after excluding two mismatches (solar illumination and viewing angle) between satellite sensors. We also found that VIs-based EOS occurred below the freezing point, while SIF-based EOS occurred above the freezing point, suggesting that SIF-based EOS is more physiologically meaningful. Our study proposed that the late VIs-based EOS was caused in part by the effect of changes in soil background on VIs and VIs-based EOS. Our results highlight the need to re-evaluate current LSP data products derived from reflectance-based VIs and to develop new vegetation phenology data products using emitted energy such as SIF.

1. Introduction

Vegetation phenology is the seasonal dynamics of plant canopy (e.g., leaf bud burst, leaf emergence, leaf senescence, leaf-off), and these various stages are sensitive to climate change and regulate carbon dynamics in terrestrial ecosystems (Adole et al., 2019; Chang et al., 2019; Piao et al., 2019; Richardson et al., 2012). Time series data from satellites have been commonly used to study vegetation phenology including the start (SOS), end (EOS), peak (POS), and length (LGS) of the growing season (Gonsamo et al., 2013; Melaas et al., 2016; Piao et al., 2019; Richardson et al., 2013; Zhang et al., 2003). Because individual pixels of satellite images often contain vegetation and non-vegetation components, land surface phenology (LSP) term is often used in the remote sensing community. LSP can be characterized from the

* Corresponding authors.
E-mail addresses: xiangming.xiao@ou.edu (X. Xiao), dongjw@igsnrr.ac.cn (J. Dong).

https://doi.org/10.1016/j.rse.2022.113209
Received 24 February 2022; Received in revised form 24 July 2022; Accepted 30 July 2022

perspectives of vegetation structure (e.g., leaf emergence, canopy dynamics, green-up) or the perspective of vegetation function or physiology (e.g., photosynthesis or GPP, net carbon exchange) (Chang et al., 2019; Jeong et al., 2017; Walther et al., 2016; Yang et al., 2019; Yin et al., 2020; Zhang et al., 2020b, 2020c). In fact, only a biologically accurate LSP estimate, whether from a structural or functional perspective, is primarily important for understanding vegetation response to climate change and carbon-water interactions, as well as improving terrestrial models (Piao et al., 2019; Richardson et al., 2012, 2013).

From the perspective of canopy structure, greenness-based vegetation indices (VIs), such as NDVI (Tucker, 1979), EVI (Huete et al., 2002), and NIRv (Badgley et al., 2017) (Eqs. 1–3), are calculated from two or more reflectance bands and are related to the fraction of absorbed photosynthetically active radiation (fPAR) (Jin and Eklundh, 2014; Badgley et al., 2017), and are used to delineate seasonal dynamics of canopy structure and photosynthetic capacity. NDVI has been widely used to monitor LSP from regional to global scales (Friedl et al., 2019; Piao et al., 2019; Tucker, 1979). From the perspective of canopy physiology, GPP and solar-induced chlorophyll fluorescence (SIF) data, referring to photosynthetic activity, have been used to estimate phenological metrics (e.g., SOS, EOS, LGS) (Garrity et al., 2011; Gonsamo et al., 2013; Joiner et al., 2013; Joiner et al., 2014; Sun et al., 2017; Xiao, 2004; Yang et al., 2019; Guanter et al., 2014; Wang et al., 2019). Spaceborne SIF has been shown to have a strong linear relationship with GPP (Sun et al., 2017, 2018; Zhang et al., 2016) at different spatial (Turner et al., 2020; Doughty et al., 2021b; Joiner et al., 2014; Lu et al., 2018; Magney et al., 2019; Wang et al., 2020b; Jeong et al., 2017; Walther et al., 2016, 2019; Wang et al., 2019) and temporal scales (Magney et al., 2019; Yang et al., 2015; Zhang et al., 2016) and across biomes (Li et al., 2018; Xiao et al., 2019; Zhang et al., 2016), and even for climate extreme events (Song et al., 2018; Sun et al., 2015; Wu et al., 2018b; Yin et al., 2020).

Most phenology studies focused on attribution and consequences analyses of phenology changes, and limited attention was given to the discrepancies between the structural and physiological proxies on phenological retrievals (Cong et al., 2017; Keenan et al., 2014; Shen et al., 2015a). Several studies found that the VIs-based phenological metrics have large discrepancies from the physiology-based ones, such as in the SOS of the snow-covered forests (Chang et al., 2019) and the EOS of the northern hemisphere (Jeong et al., 2017; Walther et al., 2016). In particular, the EOS estimates derived from NDVI are later than those derived from GPP or SIF for forests in the northern high latitude (Jeong et al., 2017; Walther et al., 2016). The seasonal decoupling between photosynthesis and greenness dynamics in boreal evergreen forests has also been reported (Jeong et al., 2017; Walther et al., 2016). One recent global study found SOS and EOS of grasslands from GIMMS NDVI (8 km), GOME-2 SIF (50 km), and GPP from the eddy flux tower sites to be inconsistent (Wang et al., 2020c). Although comparisons of SOS and EOS from VIs-SIF-GPP datasets have been investigated at the site and grid levels, the conclusions may be affected by two intrinsic differences between the SIF and VIs datasets. The first is that SIF is the emitted energy by plant while VIs is calculated from reflected energy by land surface (plants plus other surface types) (Eq. 4; Baldocchi et al., 2020; Dechant et al., 2022; van der Tol et al., 2019; Walther et al., 2016). Second is the differences in the sun-sensor geometry between SIF and VIs among satellite sensors (Doughty et al., 2019). In practice, these issues should be removed first before direct comparison. It is not clear, however, whether the discrepancy of phenological metrics from SIF and VIs datasets is related to these two factors. Recently, the near-infrared radiance of vegetation (NIRvR), was found strongly correlated with GPP and SIF during the growing season (Dechant et al., 2020, 2022; Wu et al., 2020; Zeng et al., 2022a). NIRvR is the product of NDVI and upwelling NIR radiance (NIR_{rad}) (Eq. 5), thus it is more comparable with SIF than NDVI in terms of radiance. NIRvR integrates both canopy structure and incoming radiation (Dechant et al., 2020; Zeng et al., 2019) and might be a better proxy for depicting photosynthetic seasonal dynamics than NDVI and EVI (Wu et al., 2020; Zeng et al., 2022a). However, there are limited studies on NIRvR for phenological characterization at the regional scale though previous studies have focused on the linear correlation of SIF and GPP and the slope of the SIF-GPP relationship (Dechant et al., 2022; Zeng et al., 2022a).

Furthermore, those limited available studies related to SIF-VIs comparisons only pointed out discrepancies between greenness and physiology-based phenology but did not provide empirical data to explain the problems of NDVI in the characterization of phenology. Using the correlation of meteorological variables over a period of time (e.g., season or month) to explain differences in time points (phenology) does not effectively unravel the underlying mechanisms (Jeong et al., 2017; Lu et al., 2018). In addition, previous studies that compared spaceborne SIF and VIs have several limitations, including coarse spatial and/or temporal resolutions of GOME-2 SIF data (Lu et al., 2018) and high uncertainties of GOME-2 SIF retrieval due to retrieval methods, instrument characteristics, overpass time, and viewing-illumination geometries (Wen et al., 2020). The new TROPOMI SIF data has brought unprecedented opportunities to monitor the seasonal dynamics of vegetation at higher spatial and temporal resolutions, which result in more observations and better data quality (Doughty et al., 2019; Guanter et al., 2021; Köhler et al., 2018).

Moreover, the high-altitude Tibetan Plateau, known as the Third Pole of the Earth, is also a global climate change hotspot (Chen et al., 2013; Wu et al., 2018a) where satellite-based phenology is important due to limited ground measurements. This region has experienced significant climate change and warming (Shen et al., 2013; Zhang et al., 2017a), which has caused profound changes in the structure and function of the alpine grasslands ecosystems (Chen et al., 2013; Wu et al., 2018a). In recent years, the debate over the trend of phenology in the Tibetan Plateau has attracted much attention from the community (Chen et al., 2015; Yu et al., 2010; Zhang et al., 2013). Several studies suggested that the discrepancy could be associated with the varied data (or proxies) and algorithms used (Wang et al., 2013; Zhang et al., 2013). Recently, a study found the emergence/senescence of vegetation is strongly affected by the soil background (e.g., snow cover) (Huang et al., 2021). As a result, the long-term trends in VIs-based phenology are likely to mirror changes in the phenology of snow cover and may be artifacts (Huang et al., 2021). Although previous studies have reported differences in phenology, which focused more on middle and high latitudes in Northern Hemisphere, these findings also need to be extended to high altitudes, such as in the alpine grasslands of the Tibetan Plateau. Therefore, a comprehensive and rigorous comparison of the phenological metrics from the VIs, SIF, and GPP data products is needed in alpine grasslands, which is of great significance for accurately delineating vegetation response to climate change.

To solve the above knowledge gaps, we focus on the Tibetan Plateau as our study area and explore the phenological differences and the inherent mechanism. The objectives of this paper are (1) to examine the discrepancy of phenological metrics (SOS, EOS, LGS) from greenness-based (NDVI, EVI, NIRv) and physiology-based (SIF, GPP) datasets; (2) to evaluate the reasonability derived from greenness- and physiology-based phenology in terms of biology; and (3) to investigate the mechanism explaining the discrepancy in phenology for the two kinds of indicators (greenness vs. physiology). We compared the phenological metrics (SOS, EOS, and LGS) estimated from the three vegetation indices data products (NDVI, EVI, and NIRv), GPP (GPP_{VPM}) from the Vegetation Photosynthesis Model (VPM) (Xiao et al., 2004; Zhang et al., 2017b), and the TROPOMI SIF data ($SIF_{TROPOMI}$) (Guanter et al., 2021; Köhler et al., 2018) at the site and regional scales. Furthermore, we analyzed the reliability of phenological metrics from different proxies according to the relationship between phenological metrics (SOS and EOS) and air temperature in the Tibetan Plateau, as the air temperature is an important limiting factor controlling vegetation growth and phenology (Shen et al., 2016; Shen et al., 2015b).

2. Materials and methods

All datasets were from satellite retrievals and were evaluated in 2019–2021 (see Table. S1). They were all aggregated to 0.2° spatial resolution. It should be noted that the locations of the nine eddy covariance (EC) tower sites were only used for phenological comparisons between SIF and VIs due to data unavailability during our study period in the Tibetan Plateau (see Text. S1, Table. S2 and Figs. S1-S2 for details).

2.1. MODIS land cover data

The MODIS Terra/Aqua Combined Land Cover Type product (MCD12Q1 V6) at 500 m spatial resolution was used, which includes grasslands and other land cover types, as defined by the International Geosphere-Biosphere Program (IGBP) classification scheme (Friedl and Sulla-Menashe, 2015) (Fig. S1). The alpine grasslands, dominated by alpine meadow and alpine steppe, were focused on in this study because they occupied about 50% of the Tibetan Plateau and 80% of the alpine ecosystems (Zhang, 1993). We aggregated the land cover map at 500 m spatial resolution into a new land cover map with a spatial resolution of 0.2° by using the majority rule. We kept those pixels whose vegetation types remained unchanged (always grass) during 2001–2019 to ensure that results are not affected by the changes in land cover types over years (Friedl and Sulla-Menashe, 2015).

2.2. MODIS surface reflectance and vegetation indices

Two commonly used MODIS surface reflectance (SR) products, MOD09A1 V6 (Vermote, 2015) and MCD43A4 V6 (Schaaf and Wang, 2015b) in 2019–2021 were used to generate 8-day VIs data. The native spatial resolution of both products is 500 m. We first identified and masked all pixels flagged as clouds, cloud shadows, aerosol, and snow by using the pixel quality assurance (QA) layers for MOD09A1, and BRDF/Albedo MCD43A2 band-specific quality assessment products (Schaaf and Wang, 2015a) for MCD43A4, respectively (Zhang et al., 2017b). Second, for both SR products, we calculated the normalized difference vegetation index (NDVI) (Tucker, 1979), enhanced vegetation index (EVI) (Huete et al., 2002), and near-infrared reflectance of vegetation (NIRv) (Badgley et al., 2017) (Eqs. 2–4). Third, we applied a gap-filling procedure followed by Zhang et al. (2017b) to process the VIs data and generate the completed time series data. Fourth, we aggregated these VIs data from 500 m to 0.2° spatial resolution by using a simple average method. To avoid spurious estimation of phenological transition dates when the canopy was covered with snow in the nongrowing season which was undetected by the snow flag (Piao et al., 2019; Zhang et al., 2013), those likely snow-contaminated VIs values for each pixel were replaced with a constant dormant background value, which was taken to be the median value of the all snow-free values of between November and the following March in the most recent 3 years. The daily MCD43A4 data were sampled temporally to 8-day means consistent with MOD09A1 and GPP, and SIF data.

$$NDVI = \frac{NIR_{ref} - Red_{ref}}{NIR_{ref} + Red_{ref}} \quad (1)$$

$$EVI = 2.5 \times \frac{NIR_{ref} - Red_{ref}}{NIR_{ref} + 6 \times Red_{ref} - 7.5 \times Blue_{ref} + 1} \quad (2)$$

$$NIR_v = NDVI \times NIR_{ref} \quad (3)$$

where *NDVI* is the normalized difference vegetation index, *EVI* is the enhanced vegetation index; $Blue_{ref}$, Red_{ref}, and NIR_{ref} are the reflectance values from the *Blue*, *Red*, and *NIR* bands, respectively; *NIRv* is near-infrared reflectance of vegetation.

2.3. MCD12Q2 land surface phenology data product

The land surface phenological metrics in 2019 were obtained from the MODIS Land Cover Dynamics (MCD12Q2 V6) product (Friedl et al., 2019) because the data was only through 2019. The data product was derived from the time series of the 2-band Enhanced Vegetation Index (EVI2) calculated from MODIS Nadir Bidirectional Reflectance Distribution Function (BRDF)-Adjusted Reflectance (NBAR). The SOS and EOS dates (i.e., 'Greenup', and 'Dormancy' layers in the product) were defined as the date when EVI2 first and last crossed 15% of the EVI2 amplitude in the growing cycle, respectively (Friedl et al., 2019).

2.4. SIF and TOA reflectance data from TROPOMI

The TROPOspheric Monitoring Instrument (TROPOMI) onboard the Sentinel-5 Precursor satellite (Veefkind et al., 2012) was launched into low Earth orbit on 13 October 2017 with an equatorial crossing time of 1:30 pm (local solar time) and a 17-day repeat cycle (Köhler et al., 2018). TROPOMI was configured with four spectrometers covering the wavelength of ultraviolet-visible (UV-VIS, 270 nm – 495 nm), near-infrared (NIR, 675 nm – 775 nm), and shortwave infrared (SWIR, 2305 nm – 2385 nm). The wide swath width of approximately 2600 km enables near-daily global surface coverage with a footprint size of 7 km along track and 3.5–15 km across track (i.e., 3.5 km at nadir and 15 km at the edge of the swath). Since a retrieval window ranging from 743 to 758 nm of TROPOMI covers the SIF emission spectrum which is devoid of atmospheric absorption features, and thus it allows for SIF retrieval through quantifying the change in optical depth of Fraunhofer lines (Köhler et al., 2018). Therefore, the SIF retrievals are less sensitive to atmospheric scattering by aerosols and clouds compared to VIs (Frankenberg et al., 2012). In addition, TROPOMI SIF could significantly improve the representation of the ground footprint compared with the other SIF datasets. The GOME-2 and OCO platforms are less suitable for phenological analyses at regional scales due to their lack of spatial coverage and infrequent revisit periods (Köhler et al., 2018). Specifically, the GOME-2 instruments have a coarse footprint of about 40 km × 40 km without detailed spatial patterns, although it provides continuous spatial coverage (Joiner et al., 2013). The OCO-2 SIF data does not have sufficient samples for continuous data over time with a maximum ~10 km-wide full swath, despite a better spatial resolution of single OCO-2 ground pixels (2 km × 1.3 km) (Sun et al., 2017). In contrast, TROPOMI provides near-daily spatially continuous global coverage as opposed to OCO due to its wide swath (Guanter et al., 2015; Guanter et al., 2021; Köhler et al., 2018) and has a higher spatial resolution as opposed to GOME-2 (Köhler et al., 2018). Köhler et al. (2018) produced the global ungridded TROPOMI SIF data by applying a singular value decomposition method in a 743–758 nm spectrum window with a spectral resolution of ~0.4 nm and a signal-to-noise ratio of ~2500 (Köhler et al., 2018). The comparison between TROPOMI and OCO-2 SIF shows excellent consistency (Köhler et al., 2018).

A new TROPOMI SIF data product ($SIF_{TROPOMI}$) from European Space Agency (ESA) was recently released (Guanter et al., 2021; NOVELTIS et al., 2021). This dataset provides two important variables along with SIF: one is the top of atmospheric (TOA) reflectance at atmospheric windows within 665–785 nm including the Red and NIR bands, which can generate NDVI; another is the mean TOA radiance (NIR_{rad}) in 743–758 nm fitting window. More details are described in Guanter et al. (2021). We used this data for 2019–2021. Since we now have SIF and NDVI acquired simultaneously at the sounding level using the same TROPOMI sensor, the differences in the seasonality of SIF and NDVI in this data will be completely independent of sun-sensor geometry effects and spatial and temporal sampling biases. We, therefore, conducted three experiments below. **Exp-1:** We first compared the phenological differences between MOD09A1-based NDVI, EVI, NIRv, and TROPOMI-based SIF. **Exp-2:** We then compared the phenological discrepancies between NBAR/MCD43A4-based NDVI, EVI, NIRv, and TROPOMI-based

SIF to minimize potential seasonal effects of the illumination geometry. **Exp-3:** We finally compared the phenological differences between NDVI, NIRv, and NIRvR (Eq. 5) all from the TROPOMI to remove potential intrinsic mismatches (solar illumination and sun-sensor geometry) between SIF and VIs.

In this study, soundings with a viewing zenith angle over 70° were excluded, as described for both SIF products by Köhler et al. (2018) and Guanter et al. (2021). The differences in viewing geometry are accounted for by taking 8-day averages at 0.2° spatial resolution as detailed by Doughty et al. (2021a). Coincidentally, 8-day mean SIF allows us to compare TROPOMI SIF to 8-day MODIS-based vegetation indices and GPP. We gridded 0.2° SIF data with an oversampling method (Doughty et al., 2021a; Turner et al., 2020). The method splits a footprint via its corner coordinates into a set of sub-pixels within that footprint and finds in which grid box each sub-pixel of a footprint falls, and computes the average of all points in the 0.2° gridcell (Köhler et al., 2018). To ensure the reliability of SIF data quality for analysis, we also filtered out those grid cells that contained only one single sounding or whose standard deviation was >0.6 mW m^{-2} sr^{-1} nm^{-1}. It should be pointed out that in order to weigh the cloud coverage against the number of soundings when gridding the SIF-related data (SIF retrievals and reflectance), we compared two strategies for spatial aggregation, i.e., filtering the soundings as cloud-free (clear sky) or selecting soundings with <20% cloudiness, respectively, before gridding. The satisfactory quality-check results confirmed that the SIF data are sufficient to analyze vegetation seasonal cycle and phenological metrics at 0.2° spatial resolution (see Text S2, Figs. S3, S4).

$$SIF_{obs} = \mathrm{PAR} \times \mathrm{fPAR} \times \Phi_F \times f_{esc} \tag{4}$$

$$NIRvR = NDVI \times NIR_{rad} \tag{5}$$

where SIF_{obs} is observed SIF, PAR is the photosynthetically active radiation, fPAR is the absorbed fraction of PAR, Φ_F is the fluorescence emission yield, and can be simply represented by $SIF_{obs}/NIRvR$; and f_{esc} is the canopy escape fraction; $NIRvR$ is the near-infrared radiance of vegetation, and NIR radiance (NIR_{rad}) is the observed upwelling NIR radiance by a satellite sensor.

2.5. GPP data from the data-driven models

We used the VPM GPP data (GPP_{VPM}) in 2019–2020 with a spatial resolution of 500 m and a temporal resolution of 8 days (Zhang et al., 2017b). The GPP_{VPM} data was produced by simulations of improved light use efficiency (LUE)-based Vegetation Photosynthesis Model (VPM) model (Xiao et al., 2004), driven by the MODIS vegetation indices data and climate data from the NCEP (National Centers for Environmental Prediction) Reanalysis-2 dataset. We aggregated the GPP_{VPM} data from 500 m to 0.2° spatial resolution using an average method. It needs to be noted that the GPP_{VPM} data used in this study were model products instead of field-based measurements.

2.6. Gridded air temperature data

The 2-m daily mean air temperature, daytime mean air temperature (6 am – 6 pm), and nighttime mean air temperature (6 pm – 6 am) were calculated from the gridded hourly air temperature data with a spatial resolution of 0.25° in 2019–2021 which were obtained from the European Reanalysis (ERA5) dataset (Hersbach et al., 2020). The ERA5 dataset was the fifth generation of the European Centre for Medium-Range Weather Forecasts (ECMWF) atmospheric reanalysis of global climate which was archived in the Climate Data Store (https://cds.climate.copernicus.eu). All air temperature data were aggregated to 0.2° spatial resolution by using the nearest neighbor method. Given that the air temperature varies somewhat at a daily scale, we smoothed the air temperature by using a temporal moving average of a 3-day window.

2.7. Retrievals of phenological metrics

NDVI, EVI, NIRv, NIRvR, SIF ($SIF_{TROPOMI}$), and GPP (GPP_{VPM}) data were used to estimate four phenological metrics: start of the growing season (SOS), end of the growing season (EOS), length of the growing season (LGS), and the peak of the growing season (POS). For each data, >75% of the data must be available over the period pixelwise, and the missing/masked values were first filled using the cubic spline interpolation, and then the noisy data (outliers and spikes) which are likely caused by clouds and poor atmospheric conditions in the original time series were filtered out by the weighted Savitzky-Golay (S-G) filter (Chen et al., 2004; Yang et al., 2019). The central point of the three-point moving window was double-weighted if it is within ±25% of the median of the moving window (Walther et al., 2016). The filtering process makes the input data into the following fitting model more stable, especially for the high-noise fluctuant SIF values during the winter dormant period (Walther et al., 2016). Subsequently, a seven-parameter double logistic function smoothing method (Eq. 6) proposed by Gonsamo et al. (2013) was performed to objectively smooth and reconstruct the above gap-filled time-series data (with an 8-day interval) to the daily ones (Gonsamo et al., 2013; Yang et al., 2019).

$$f(t) = \alpha_1 + \frac{\alpha_2}{1 + e^{-\partial_1(t-\beta_1)}} - \frac{\alpha_3}{1 + e^{-\partial_2(t-\beta_2)}} \tag{6}$$

where $f(t)$ represents the NDVI observations at a given day of year (DOY) (t). α_1 is the background NDVI value in the winter dormant period, α_2 and α_3 are the amplitudes in the periods of 'spring-early summer plateau' and 'late summer-autumn plateau', respectively. β_1 and β_2 are the midpoints (in DOYs, similar to the first derivatives) of growth curve transitions for the green-up phase and brown-down phase, respectively, and ∂_1 and ∂_2 are the slope coefficients of the growth curve at β_1 and β_2 transition dates, respectively.

The phenological metrics of the time series were estimated by using a relative threshold method (Wu et al., 2013; Yang et al., 2019), that is, the SOS and EOS dates were defined as the first and last dates at which 15% of the amplitude (maximum-minimum) of smoothed daily time series (SIF, GPP, and VIs) were reached. The 15% threshold is consistent with MCD12Q2 V6 phenology products. The POS was identified as the first day (DOY) at which the fitted daily time series reached its peak (Yang et al., 2019). The LGS was defined as the difference between the SOS and EOS dates (LGS = EOS – SOS).

3. Results

3.1. Phenology as indicated by SIF, GPP, NDVI, EVI, and NIRv relative to air temperature

It should be noted that all results in the main text are illustrated for 2019 as an example since the results are consistent for 2019–2021 (see Supplementary Figures). We analyzed the seasonal dynamics of SIF, GPP, NDVI, EVI, and NIRv which VIs are from the MCD43A4 dataset at the site-averaged level to examine their seasonal consistency (Fig. 1). We found that SIF has higher temporal consistency with GPP than NDVI, EVI, and NIRv, which is more pronounced in the normalized data (Fig. 1 e). In the spring, NDVI started to rapidly rise on DOY 130, which was earlier than SIF (DOY 144), but in the fall, NDVI instantly dropped to its lowest value on DOY 305, which was later than SIF (DOY 275) (Fig. 1 a). The SOS and EOS dates from GPP and SIF were very close, also the LGS from GPP was similar to those from SIF (Fig. 1 d, e). Meanwhile, the SOS dates from VIs (NDVI, EVI, and NIRv) were slightly earlier than those from SIF (or GPP), but the EOS dates from VIs were substantially later than those from SIF (or GPP) (Fig. 1 b, c).

We investigated the responses of SIF, GPP, NDVI, EVI, and NIRv to mean air temperature (i.e., daily, daytime, and nighttime, Figs. 1, S5-S6) at the site-averaged level to identify the threshold values of air

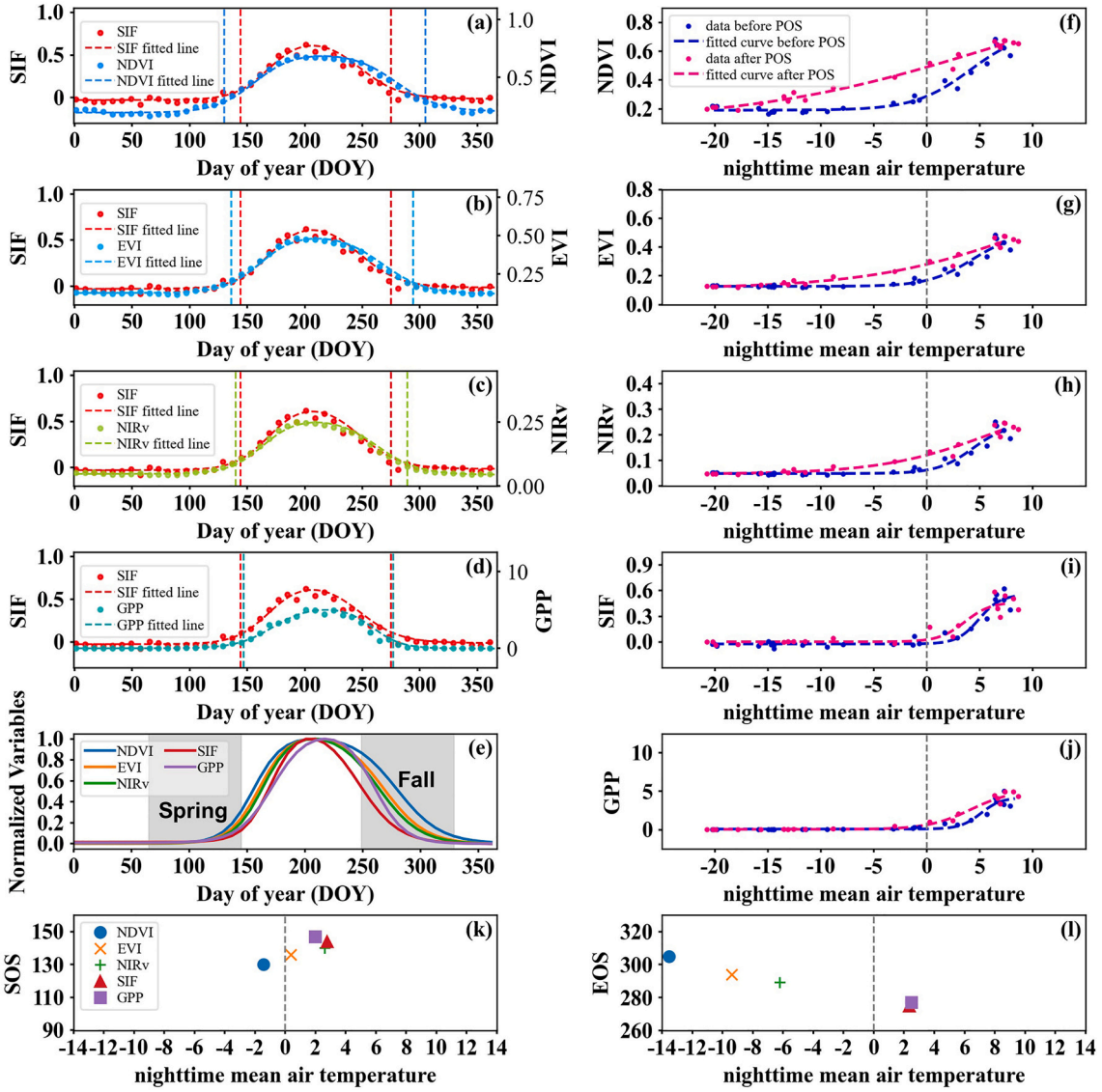

Fig. 1. The site-averaged seasonal dynamics of TROPOMI SIF, MCD43A4-based VIs (NDVI, EVI, NIRv), and VPM GPP and their relationships with nighttime mean air temperature in 2019 across nine eddy flux tower sites in the Tibetan Plateau, China. The dots and dashed curves in the left panel (a-d) represent the indices (SIF, VIs, and GPP) values and corresponding fitted curves, respectively, and vertical lines represent the start (SOS) and end (EOS) of the growing season. The indices (SIF, VIs, and GPP) values normalized using the annual maximum and minimum are fitted (e). The blue and red dots in the right panel (f-j) indicate the data (indices and air temperature) before the peak of the growing season (POS) and after POS, respectively, dashed curves represent the fitted curves. The scatter plots (k, i) indicate the relationships between the air temperature and SOS and EOS dates for individual indices. While NDVI, EVI, and NIRv are unitless quantities, GPP is shown in units of g C m^{-2} day^{-1}, SIF in units of nW m^{-2} nm^{-1} sr^{-1}, SOS/EOS in units of day of year (DOY), and air temperature in units of °C. (For interpretation of the references to colour in this figure legend, the reader is referred to the web version of this article.)

temperature, at which VIs (NDVI, EVI, NIRv), SIF, and GPP start to rise in spring (related to SOS) and drop to their lowest values in fall and winter (related to EOS) (Fig. 1 f-j). Fig. 1 f-j shows the data in two time periods: (1) data before the peak date of the growing season (hereafter, POS), and (2) data after the POS. SIF and GPP started to rise after the three temperature variables reached above 0 °C and dropped to their lowest values when nighttime air temperature approached 0 °C. In comparison, NDVI started to rise when the nighttime air temperature was still below 0 °C and all three vegetation indices did not drop to their lowest values when the three air temperature variables were already below 0 °C (Fig. 1 f-j). The scatter plots between the air temperature and SOS and EOS dates show that SOS and EOS dates from the vegetation indices are not physiologically reasonable, as plants stop photosynthesis when air temperature, particularly nighttime air temperature, is several degrees below freezing (Fig. 1 k, l).

Similar results of seasonal dynamics of all indices and the responses of indices to mean nighttime air temperature at the region-averaged level were found for the MCD43A4 datasets (Fig. S7). Similar results were found for the MOD09A1 (Figs. S8-S11) and TROPOMI datasets (Fig. 2, Figs. S12-S14) at the site-averaged and region-averaged levels on the plateau, respectively. The results of the MOD09A1 product were very similar to those of MCD43A4. All data products showed consistent discrepancies between VIs and SIF/GPP. Compared to NDVI, smaller differences for NIRv and NIRvR in the TROPOMI dataset were shown (Fig. 2 a-d).

3.2. *Spatial distribution of phenological metrics in the Tibetan Plateau derived from SIF, GPP, and vegetation indices*

We calculated the differences of phenological metrics (SOS, EOS, LGS) between SIF and MCD43A4-based VIs and GPP for individual grid cells in the Tibetan Plateau and examined their spatial distributions and

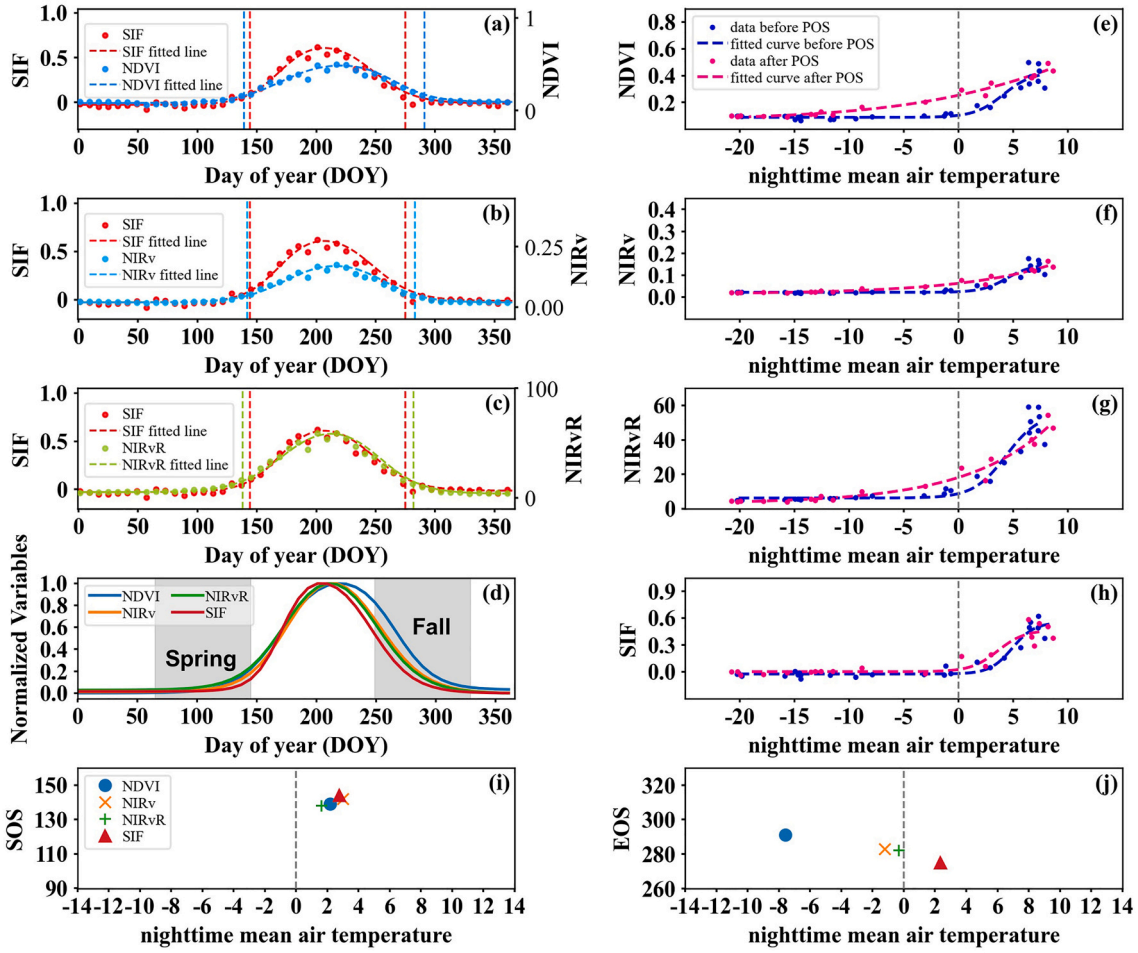

Fig. 2. Similar as Fig. 1 but for TROPOMI-based SIF, NDVI, NIRv, and NIRvR and their relationships with nighttime mean air temperature. While NIRvR is shown in units of nW m^{-2} nm^{-1} sr^{-1}.

histograms of the difference values (Figs. 3-4, S15-S16). The differences of SOS, EOS, and LGS between SIF and GPP have normal distributions with a center around zero (Fig. 3). The differences of SOS between SIF and VIs also have a normal distribution with a center around zero, but that of EOS has a normal distribution with a large departure from zero (~15 days). The differences of LGS between SIF and VIs were more remarkable than those of SOS and EOS (up to 75 days) (Figs. 3, S15). Apparent differences in SIF- and VIs-derived phenological metrics (SOS, EOS, and LGS) occurred in over 90% of all the pixels in the study area, most of them distributed in the eastern and southwest Tibetan Plateau (Fig. 3). As a result, the LGSs derived from NDVI, EVI, and NIRv were much longer (even up to ~40 days) than those from SIF or GPP (Figs. 4, S15).

Similar results on the phenological differences between SIF and VIs as well as GPP were found for the MOD09A1 (Figs. S17-S20) and TROPOMI datasets (Figs. 5, S21-S23) at the site-averaged and region-averaged level. The results for the years 2020 (Figs. S24-S26) and 2021 (Figs. S27-S29) were consistent with the ones in 2019. Also the results of the soundings gridding from the clear sky and cloud fraction ≤20% showed a very consistent pattern despite the slight differences (Figs. S30-S35). That evidence suggests our robust conclusion. Therefore, we only showed the results from the rule that the cloud fraction is <20% in the main text.

We investigated the relationships between phenological metrics (SOS and EOS) and air temperature for all grid cells in the Tibetan Plateau in 2019 for the MCD43A4 dataset. In terms of SOS, the histograms of the three air temperature variables have similar distributions among the five indicate-derived SOS dates (Figs. 6, S36-S37). In terms of EOS, the histograms of the three air temperature variables from the vegetation indices (NDVI, EVI, and NIRv) differ substantially from those of SIF and GPP (Figs.7, S38-S39). For most of the gridcells (> 88%) in the study area, the air temperature at the VIs-derived EOS was several degrees below 0 °C (Fig. 6). As the leaves of Tibetan Plateau grasses are likely to cease photosynthesis when the air temperature drops below 0 °C, the VIs-derived EOS estimates are not consistent with our basic understanding of photosynthetic responses to temperature. In comparison, air temperature at the EOS dates from SIF and GPP data are mostly above 0 °C, which is more physiologically realistic (Figs.7, S40). Additionally, we found that EOS dates from the MODIS standard phenology products (MCD12Q2 V6) are also in the dates with air temperature below zero (Figs. 7b).

Similar results on these phenology-temperature relationships were found for the MOD09A1 (Figs. S41-S46) and TROPOMI datasets (Figs. 8, S47-S51). Both EVI and NIRv for all sensors have fewer pixels at sub-zero temperatures than NDVI; The TROPOMI-derived NIRv and NIRvR show fewer pixels at sub-zero temperatures compared to the other two sensors. Also, the results from the grided TROPOMI data from soundings with clear sky and cloud fraction ≤20% showed a consistent pattern (Figs. S52-S55).

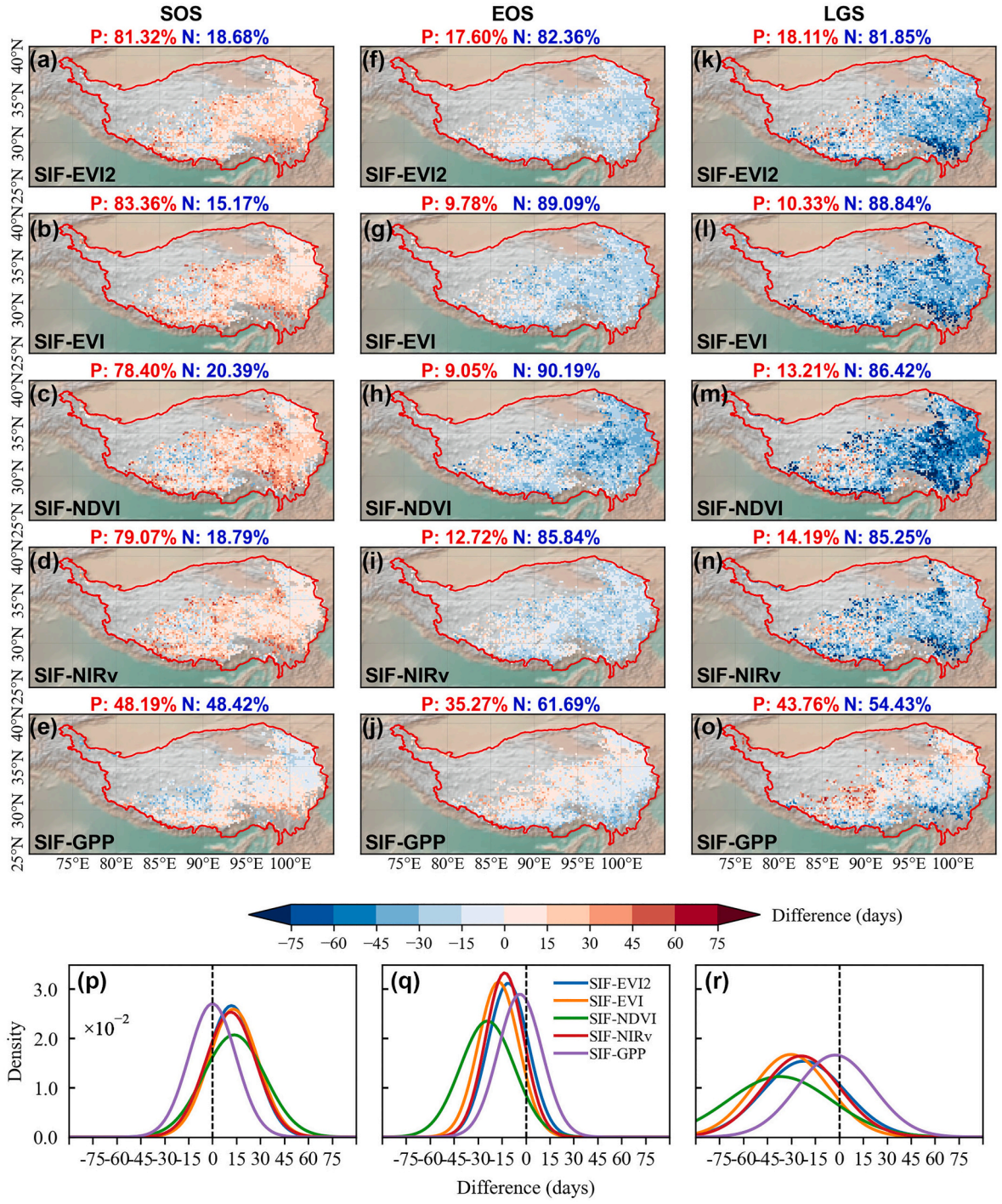

Fig. 3. Spatial distributions and histograms of the phenological differences between TROPOMI SIF and EVI2 (MCD12Q2 V6), MCD43A4-based VIs (EVI, NDVI, NIRv), and VPM GPP in 2019 in the Tibetan Plateau, China. The left, middle, and right panels indicate spatial distributions of phenological differences on the start (SOS, a-e), end (EOS, f-j), and length (LGS, k-o) of the growing season, respectively. The red and blue colors denote the percentage of positive (P) and negative (N) differences of phenological metrics between EVI2, EVI, NDVI, NIRv and GPP against SIF, respectively. The lower panel (p-r) indicates histograms of the phenological differences. The vertical dashed lines mean the difference of phenological date is zero (days). The Density denotes the probability density of the differences. (For interpretation of the references to colour in this figure legend, the reader is referred to the web version of this article.)

4. Discussion

4.1. SOS estimates and discrepancy

A recent study compared SOS estimates from NDVI and GOME-2 SIF for forests in northern high latitudes and reported that NDVI-based SOS dates (SOS_{NDVI}) were weeks earlier than SIF-based SOS dates (SOS_{SIF}) (Jeong et al., 2017). The authors claimed that later SOS_{SIF} dates were due to the delay associated with the photosynthetic activity. In our study of alpine grasslands in the Tibetan Plateau, we also found that SOS_{NDVI} dates were two weeks earlier than SOS_{SIF} dates (Figs. 1, 2, 3, 5). This could be attributed to the early rise of NDVI due to the dynamics of snow and/or soil moisture (wetness).

During the transition from winter to spring, the land surface

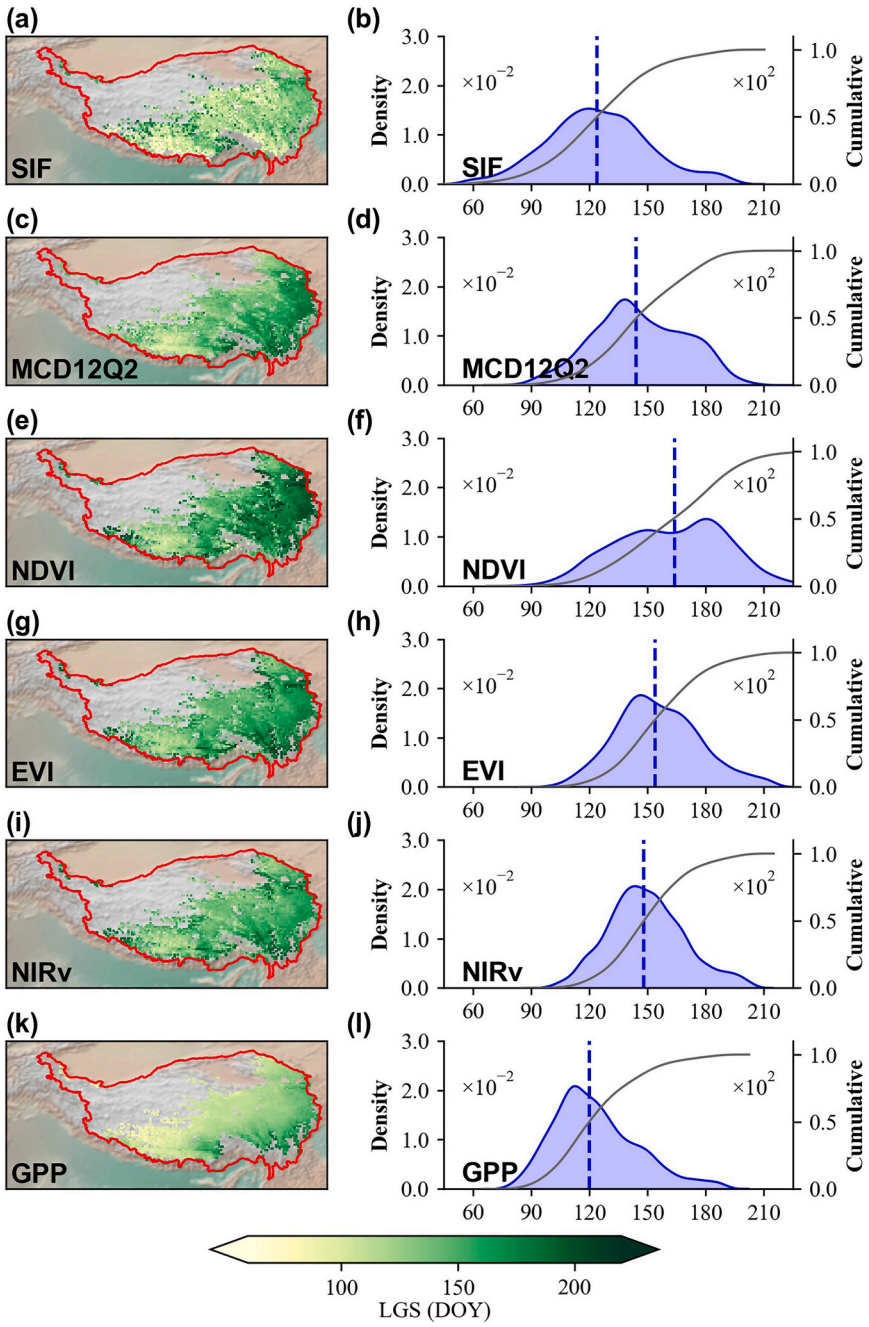

Fig. 4. Spatial distributions and histograms of the length of the growing season (LGS) in 2019 in the Tibetan Plateau, China. Each row represents individual indices, TROPOMI SIF (a, b), MCD12Q2 V6 (c, d), MCD43A4-based NDVI (e, f), EVI (g, h), NIRv (i, j), and VPM GPP (*k*,*l*), respectively. The left and right panels indicate the spatial and frequency density distribution of the LGS derived from individual indices. Blue vertical dashed lines and gray curves in the right panel indicate mean values and the cumulative distributions of LGS, respectively. (For interpretation of the references to colour in this figure legend, the reader is referred to the web version of this article.)

dynamics in the Tibetan Plateau can be generally divided into four stages over time: (1) snow-covered soils and dead leaves, (2) wet soils and land surfaces and dead leaves after snowmelt, (3) dry soil surface and dead leaves, and (4) new leaf emergence and canopy green-up (Fig. 9). In stage 1, snow is observed by satellite sensors and NDVI values from satellites are very low. In stage 2, soil moisture starts to increase when snow melts and wet soil surface and dead leaves are observed by sensors, thus NDVI values remain low but higher than stage 1 (Smith et al., 2019; Zhang et al., 2020a). In stage 3, when the air temperature rises, the soil surface and dead leaves dry up and have much higher NDVI values than stage 2, as dry soils have higher NIR and visible (VIS) reflectance than wet soils (Smith et al., 2019; Nagler et al., 2000; Lekner and Dorf, 1988; Tian and Philpot, 2015). In stage 4, new leaves emerge after air temperature rises above 0 °C (Figs. 1), and the chlorophyll of the canopy starts to absorb light, emit SIF, and conduct photosynthesis (GPP). Thus, the timing of leaf emergence (green-up), SIF, and GPP are consistent. We argue the SOS_{NDVI} dates reflect the land surface changes from stage 2 to stage 3 (Fig. 9 b). Satellite observations at the landscape level are affected by soil background during the transition from dormancy to the green-up phase (Walther et al., 2016; Wang et al., 2013), especially the snowmelt and drying processes, which cause an early rise of NDVI and early SOS_{NDVI} estimates with the air temperature being below 0 °C (Chang et al., 2019; Ensminger et al., 2008). A recent study in the Tibetan Plateau found that an earlier SOS_{NDVI} estimate is affected by earlier snowmelt, which would attribute to an advance in SOS estimate as an artifact of snow cover changes (Huang et al., 2021). In our study, the finding that VIs-based SOS of about half the area occurred below the freezing point also proves the bias of land surface SOS estimates. Thus, the effects of soil background, especially soil moisture, could be an important reason for the earlier SOS dates from the VIs-based approach.

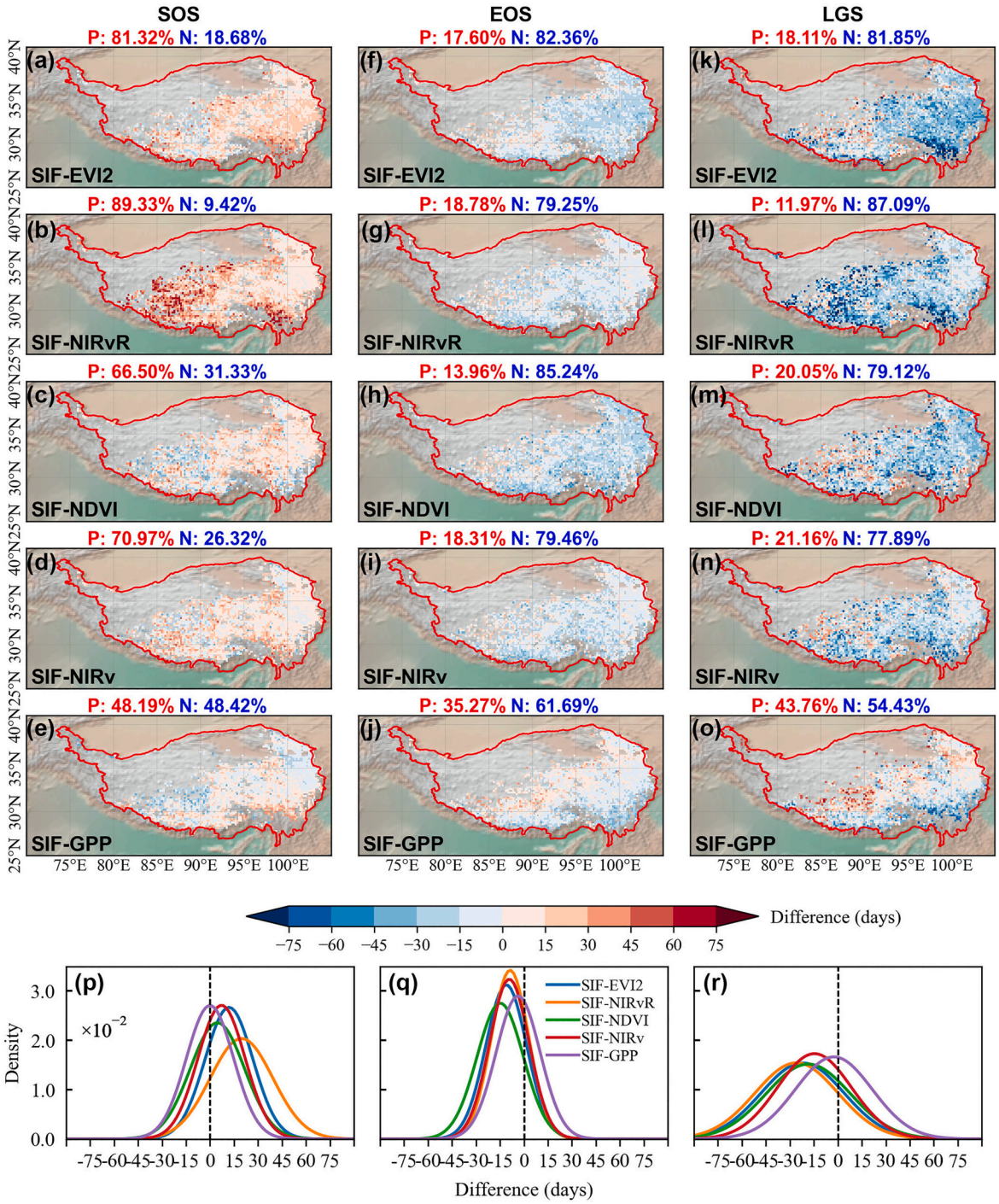

Fig. 5. Similar as Fig. 3 but for TROPOMI SIF and EVI2 (MCD12Q2 V6), TROPOMI-based VIs (NIRvR, NDVI, NIRv), and VPM GPP.

4.2. EOS estimates and discrepancy

Several studies analyzed GOME-2 SIF and NDVI data for various forests and reported that SIF-based EOS dates (EOS_{SIF}) are weeks (to months) earlier than NDVI-based EOS dates (EOS_{NDVI}) (Jeong et al., 2017; Wang et al., 2020c). Our study of alpine grasslands in the Tibetan Plateau also shows that EOS_{SIF} is two months earlier than EOS_{NDVI} (Fig. 1). During the transition from fall to winter, the land surface dynamics in the Tibetan Plateau can also be generalized into four stages over time (Fig. 9): (1) green vegetation, (2) senescent vegetation (dead but most of the leaves still in the canopy), (3) leaf fall and exposed wet soil surface, and (4) snow-covered dead leaves and soils (Fig. 9). In stage 1, green leaves are observed by satellite sensors and NDVI values are high. In stage 2, dry and dead leaves in the canopy are observed by satellite sensors and NDVI values are lower than stage 1 while GPP and SIF approach 0. In stage 3, wet soil surface and dead leaves on the ground are observed by satellite sensors and NDVI values are much lower than stage 2. In stage 4, snow cover results in the lowest NDVI values.

We assume that the EOS_{SIF} dates reflect the land surface in stage 2, but EOS_{NDVI} dates are likely to relate to the land surface changes between stages 2 and 3 (Fig. 9). The difference in EOS between VIs and SIF datasets is mostly related to the mathematical models that use VIs to estimate EOS. Plant senescence is a natural and slow-process, and dead

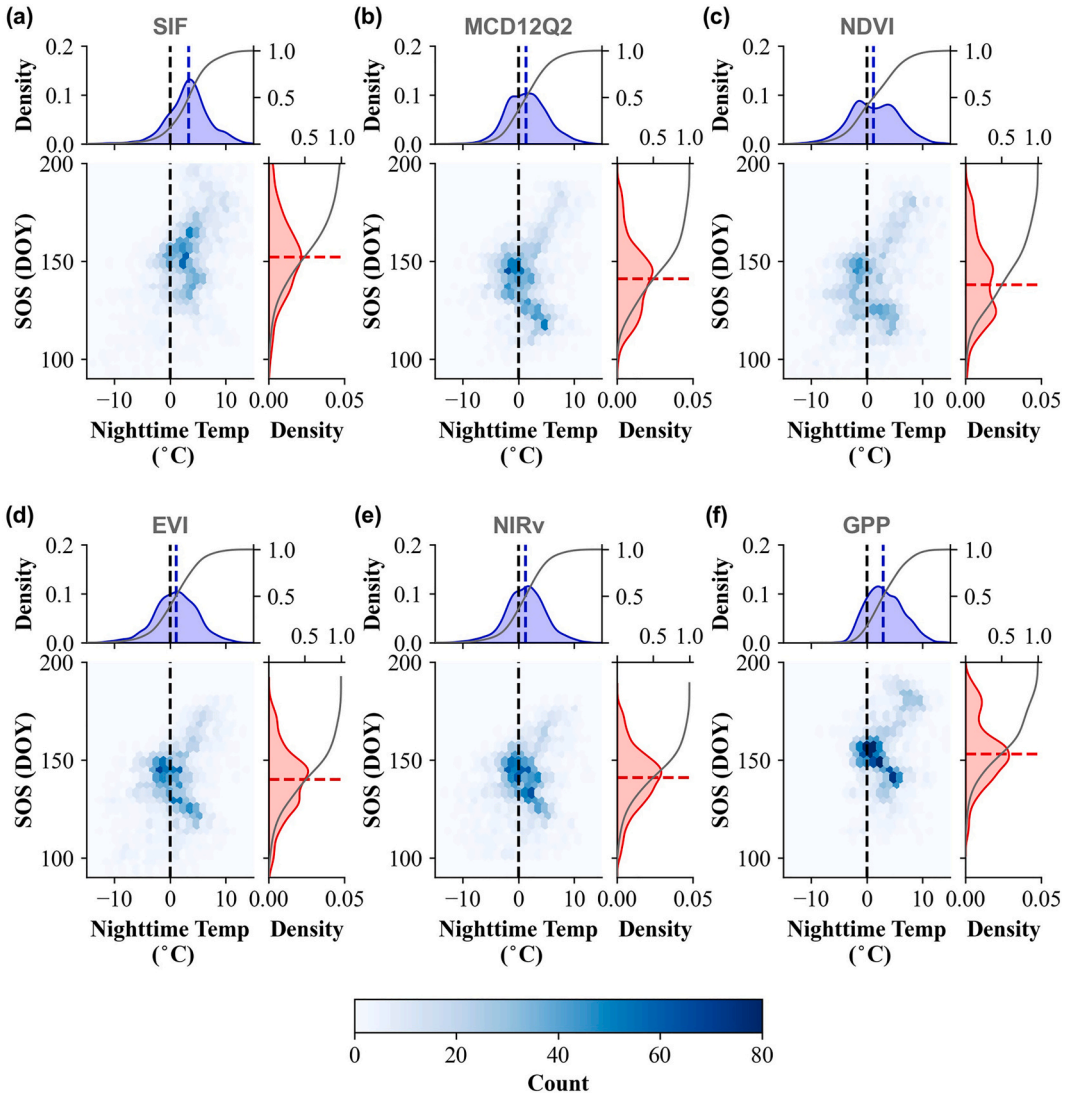

Fig. 6. Summary of the start of the growing season (SOS) from six indices and their relationships with nighttime mean air temperature in 2019 in the Tibetan Plateau. The nighttime mean air temperature (Nighttime Temp) represents the nighttime mean air temperature at the SOS date derived from TROPOMI SIF (a), MCD12Q2 V6 (b), MCD43A4-based NDVI (c), EVI (d), NIRv (e), and VPM GPP (f), respectively. In each subplot, the lower-right and upper plots represent 1-D histograms of SOS and corresponding nighttime mean air temperature across all 0.2° grid cells, respectively, while the lower-left plot represents a 2-D density heatmap indicating the distributions/relationships between SOS and corresponding nighttime mean air temperature. Red and blue dashed lines indicate mean values of SOS and corresponding nighttime mean air temperature, respectively, while gray curves indicate the cumulative distributions of nighttime mean air temperature. Black vertical dashed lines indicate 0 °C of nighttime mean air temperature. (For interpretation of the references to colour in this figure legend, the reader is referred to the web version of this article.)

plants/standing litter have similar spectral properties as the soils, thus it is hard to determine EOS from VIs dataset (Smith et al., 2019; Fig. 9). The effects of plant senescence and soils on surface reflectance could be an important reason for the later EOS dates from the VIs datasets. Previous studies only pointed out the differences between SIF and NDVI (Jeong et al., 2017; Lu et al., 2018; Wang et al., 2020c), and attributed later EOS_{NDVI} than EOS_{SIF} to the fact that photosynthesis shut down before leaf senescence in response to biophysical constraints (Jeong et al., 2017; Wang et al., 2020c), but this explanation is still insufficient to justify EOS_{NDVI}. Our work states that EOS_{NDVI} is not reasonable when the air temperature is considered. The senescence timing of annual plants and deciduous plants is controlled by their life clock or environment (e.g., air temperature). Air temperature in EOS_{SIF} and EOS_{GPP} dates is close to 0 °C, and the leaves have stopped photosynthesis at this time, indicating that EOS_{SIF} and EOS_{GPP} are reasonable in terms of biology. Air temperature before EOS_{NDVI} date is already below zero for many days, indicating that EOS_{NDVI} is not reasonable in terms of biology.

This study investigated both vegetation phenology and land surface phenology, which are two concepts that are relevant but not identical. SIF is the energy emitted by plants, and it is not or little affected by other land surface types (Badgley et al., 2017; Zeng et al., 2022b) and is less sensitive to thin clouds (Dechant et al., 2022). SIF and GPP are mostly about vegetation phenology. Currently, most attention has been given to the rapid use of SIF to calculate GPP, but the use of high spatiotemporal SIF (e.g., TROPOMI) in vegetation phenology has been neglected (Dechant et al., 2022; Zeng et al., 2022a). Our findings show that the TROPOMI SIF product has the potential to serve as a proxy for alpine grassland photosynthetic phenology with high spatiotemporal resolution. However, air temperatures were below 0 °C for VIs-derived EOS dates suggesting that the use of remotely sensed greenness indices for identifying vegetation phenology is likely to deviate from actual photosynthetic activity (Figs. 6-8). Given that both NDVI and EVI data are widely used to produce local, regional, and global-scale LSP data products (e.g., MCD12Q2 V6) (Joiner et al., 2014; Piao et al., 2019;

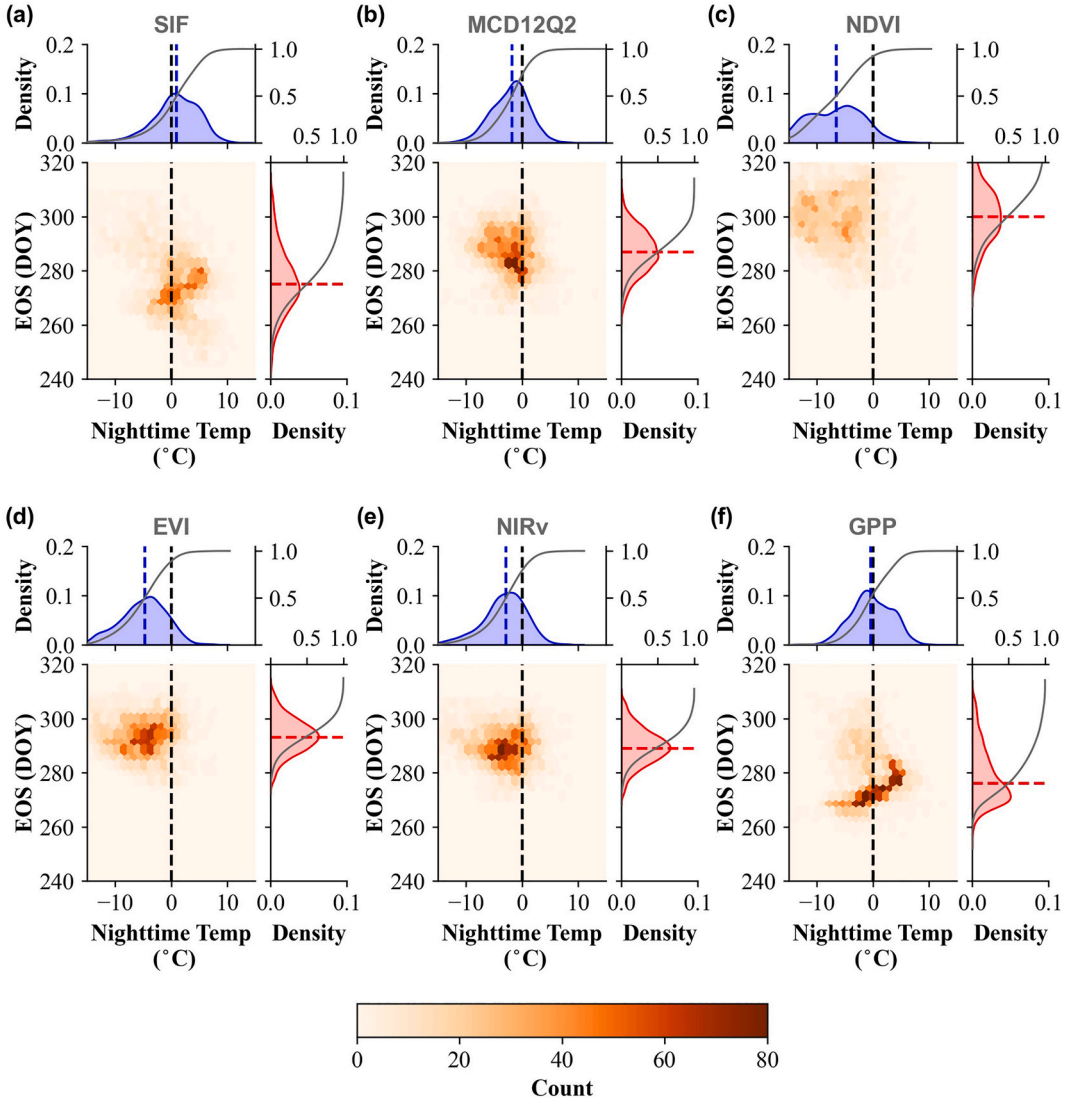

Fig. 7. Similar as Fig. 6 but for the nighttime mean air temperature at the end of the growing season (EOS) derived from TROPOMI SIF (a), MCD12Q2 V6 (b), MCD43A4-based NDVI (c), EVI (d), NIRv (e), and VPM GPP (f), respectively.

Richardson et al., 2012), the combination of later EOS and longer LGS derived from VIs datasets with some arithmetic-based phenology extraction algorithms (at least ≤15% dynamic threshold) may hinder efforts to model terrestrial productivity and predict climate change impacts on vegetation and carbon balance (Anav et al., 2015; Richardson et al., 2012; Xia et al., 2015; Sun et al., 2017). Therefore, there is an urgent need to re-evaluate these VIs-based phenology data products and re-assess their effects on our understanding of the spatiotemporal changes in vegetation carbon and water fluxes in the past four decades. SIF can be used as a caliber and/or reference for the remote sensing community to re-evaluate and validate the phenological data products derived from VIs (Magney et al., 2020).

4.3. Temperature control of land surface phenology (vegetation phenology)

The SOS and EOS need to be within the time period with air temperatures higher than 0 °C to avoid damage to plants from frozen temperatures (Noormets, 2009; Wu et al., 2014; Pierrat et al., 2022; Chang et al., 2019). If a plant is continuously exposed to a cold air temperature below the freezing point for many days, the liquid water in the leaves will be in the form of an ice-water mixture or ice, and the hydraulic system in the plant is thus blocked and photosynthesis is unable to take place. Many studies based on in situ EC flux observations (Chang et al., 2019; Pierrat et al., 2022), agree with our study (Figs. 1, S40), and they found that photosynthesis does not start until the air temperature exceeds the freezing point. Moreover, the temperature threshold (e.g. 0 °C) has been adopted by light-use-efficiency models (e.g., VPM) (Zhang et al., 2017a, 2017b), and process-based models like the Terrestrial Ecosystem Model (TEM) studies (Aber et al., 1996; McGuire et al., 1992; Raich et al., 1991). In accordance with the above empirical evidence, we found that both TROPOMI SIF and GPP_{VPM} were suitable indicators of the start and end dates of photosynthesis in alpine grasslands (Figs. 1, 2, S5-S14, S40). Our study assessed the phenological transition dates retrieved from SIF and VIs and showed that the EOS dates from VIs data need to be evaluated with air temperature data over a larger area and across vegetation types in combination with in-situ EC flux and SIF observations to make it robust.

In theory, SIF contains unique physiological information in the form of fluorescence quantum yield (Φ_F) (Magney et al., 2019). Φ_F is thought to explain the faster and stronger stress response of SIF compared to structural variables such as APAR, NDVI, or EVI (Dechant et al., 2020; Wang et al., 2020a; Zeng et al., 2022a). Dividing SIF by NIRvR results in a calculation of SIF yield (NIRvR-derived SIF_{Yield}; Eq. 5) and is an

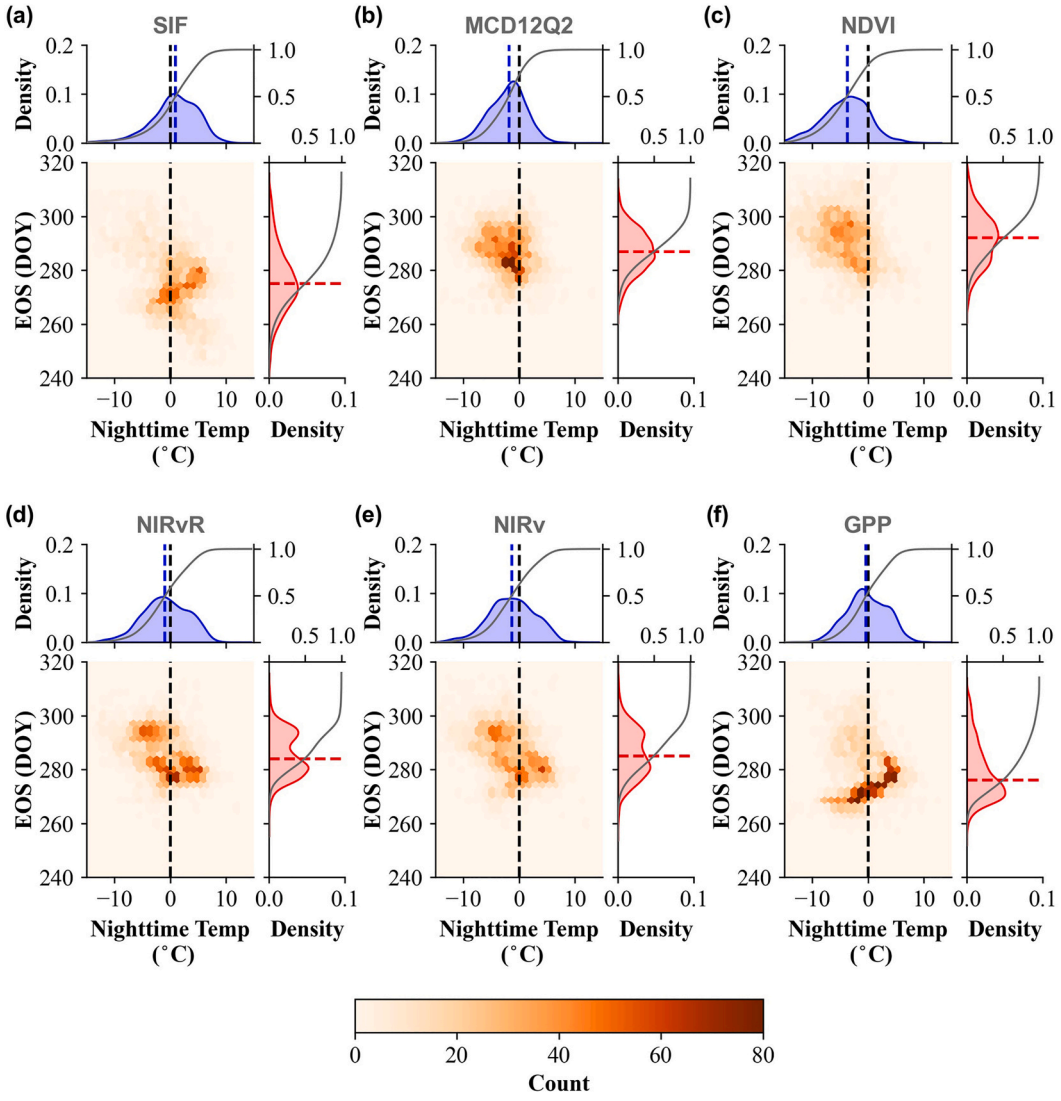

Fig. 8. Similar as Fig. 6 but for the nighttime mean air temperature at the end of the growing season (EOS) derived from TROPOMI SIF (a), MCD12Q2 V6 (b), TROPOMI-based NDVI (c), NIRvR (d), NIRv (e), and VPM GPP (f), respectively.

approximation of Φ_F. Interestingly, in this study, the NIRvR-derived SIF_{Yield} indirectly confirms that the SIF-estimated phenology is reasonable. The seasonal variation of SIF_{Yield} in the Tibetan Plateau grasslands is obvious, although the magnitude is small (Figs. 10, S56-S57). SIF_{Yield} is <0 when MODIS-based SOS_{NDVI}/EOS_{NDVI} occurs, while SIF_{Yield} > 0 when TROPOMI-based SOS_{SIF}/EOS_{SIF} occurs. We found that SIF_{Yield} was very close to the air temperature during the senescence (Fig. 10). SIF_{Yield} represents physiological photosynthetic activity related to light energy efficiency, which can partially reflect the influence of air temperature on photosynthesis. The seasonal variance of SIF_{Yield}, especially on EOS, implies that SIF_{Yield} plays an important role at 8-day time scales, which is likely sensitive to air temperature through the dynamics changes relative to plant abiotic stresses, such as low temperature or short photoperiod (Wang et al., 2020a; Zeng et al., 2022a). Our results illustrate that the TROPOMI satellite could capture the signal of alpine grassland Φ_F, that is, NIRvR-derived SIF_{Yield} can capture the rapid response of vegetation to environmental stress, highlighting its unique ability to track the seasonality of photosynthesis, when in particular, instantaneous PAR measurements are not available. Thus, in addition to NIRvR, SIF_{Yield} is also crucial for the phenological characterization of alpine grasslands. It is also worth noting that the current method of calculating SIF_{Yield} is still subject to significant uncertainty, which is directly influenced by the NDVI. SIF_{Yield} fluctuates greatly in the spring green-up period, which is mainly due to the relatively high SIF noise related to the low signal quality of SIF_{obs} (Wang et al., 2020a). Therefore, reliable estimation of SIF_{Yield} would be a key step in establishing a better link between SIF and GPP as well as delineating biome-specific phenology at leaf and canopy levels across vegetation types and under different abiotic stresses (Zeng et al., 2022a, 2022b).

4.4. *Potentials of TROPOMI-based NIRvR on vegetation phenology*

Interestingly, the MODIS-related EVI and NIRv yielded similar phenological patterns to NDVI (both MOD09A1 and MCD43A4), showing that EVI or NIRv did not show a significant advantage over NDVI in the Tibetan Plateau, although there is a slight improvement (Figs. 1, 3, S5-S11, S18). That is, there are still EOS differences between SIF and NDVI-like VIs (EVI or NIRv) on MODIS-like sensors. Also, these nearly identical results between MCD43A4 and MOD09A1 datasets suggest that the SOS/EOS discrepancy between SIF and VIs may not be due to the absence of view angle effect (BRDF) correction in MOD09A1. Similar to SIF, NIRvR based on TROPOMI outperforms NDVI (Figs. 2, 5, S12-S14), which means that radiation-involved NIRvR on the TROPOMI sensor can largely depict the EOS date (Eqs. 3–5), and TROPOMI-derived

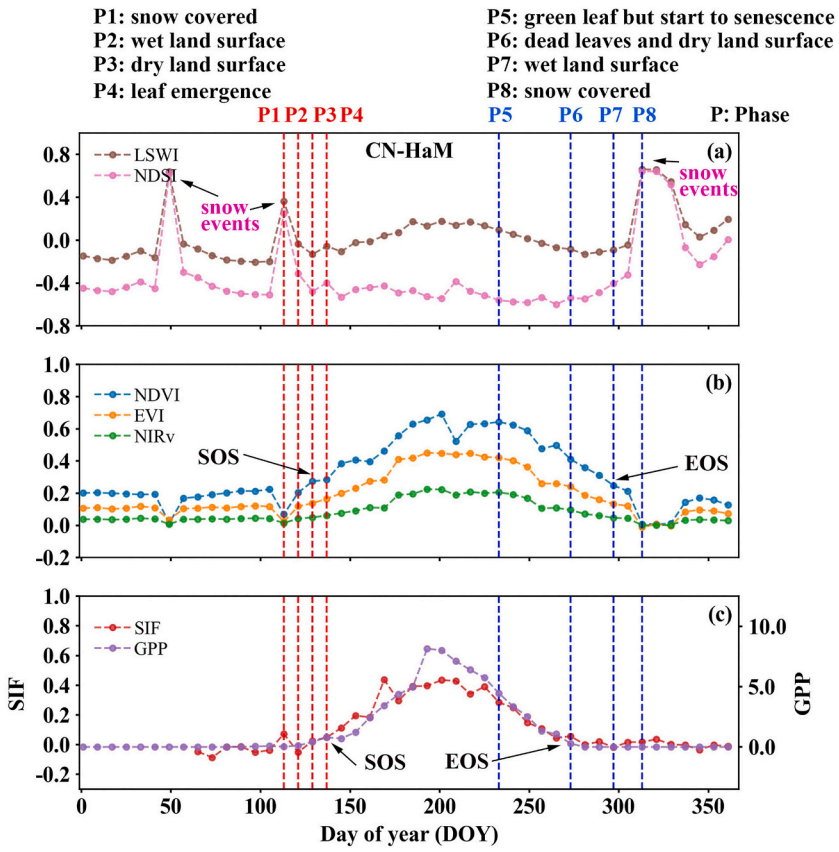

Fig. 9. The four phases (stages) of land surface dynamics during winter to spring transition (P1-P4) and from fall to winter transition (P5-P8) at one grid cell (0.2°) in the Tibetan Plateau, China. (a) LSWI (Land Surface Water Index, indicating the surface moisture status) (Xiao et al., 2002) and NDSI (Normalized Difference Snow Index, indicating the presence of fresh snow when larger than 0.4) (Riggs et al., 2017). (b) Time series of NDVI, EVI, and NIRv are derived from MOD09A1 V6 data product while (c) SIF and GPP are derived from TROPOMI SIF and VPM-based GPP data products, respectively. While LSWI, NDSI, NDVI, EVI, and NIRv are unitless quantities, GPP is shown in units of g C m^{-2} day^{-1}, SIF in units of nW m^{-2} nm^{-1} sr^{-1}, SOS/EOS in units of day of year (DOY), and air temperature in units of °C.

NIRvR yields key insight into phenological discrepancy between VIs and SIF. The difference between SIF and NDVI is the NIR radiance × Φ_F (Eq. 5). The smaller difference (NIRvR still later) between SIF and NIRvR on EOS compared to NDVI suggests that NIR radiance (NIR_{rad}) largely explains the SIF-NDVI discrepancy, which implies that the canopy structure and radiation component of SIF (i.e. APAR × f_{esc}) can constrain the slow change in NDVI before it enters dormancy in the fall (Eq. 5, Figs. 2, 5, S12-S14). Our finding also suggests the potential of NIRvR on EOS retrievals and unraveling SIF-VIs discrepancy, which is consistent with several recent studies that show that NIRvR is a robust proxy for SIF across ecosystems, spatial and temporal scales, and instrument platforms (Dechant et al., 2020, 2022; Zeng et al., 2022a). Combining the NIRvR and Φ_F that depicts the plant's response to temperature, SIF more accurately characterizes the phenological period of alpine grasslands. This is important because the current phenological retrievals based on NDVI show a greater divergence in autumn phenology compared with spring phenology.

From the perspective of SIF applications, the SIF/NIRvR ratio (SIF_{Yield}) can be used to estimate the physiological component of SIF (Φ_F), but Φ_F estimation amplifies the retrieval noise of SIF (Dechant et al., 2020). Notably, while the difference between SIF and NIRvR in SOS was not significant in 2020–2021 (Figs. 26, 29), TROPOMI data showed a positively skewed distribution of SIF-NIRvR difference in SOS in 2019 (Fig. 5 p) at the pixel scale, indicating that, unlike croplands, NIR radiance (NIR_{rad}) in alpine grasslands had a large variation in SOS and thus result in SOS_{NIRvR} does not approach SOS_{SIF} well (Eq. 5; Dechant et al., 2020). This is probably due to the complicated effects of the change of soil background on the NIR radiance (NIR_{rad}) before leaf emergence. Therefore, air temperature (Jeong et al., 2017; Lu et al., 2018) or soil moisture (Wang et al., 2019) may explain the phenological difference between SIF and NDVI. There is still a gap in time between SIF and NIRvR, with NIRvR being later. This may be because, alpine grassland photosynthesis is controlled by air temperature, and NIRvR should not contain temperature information except for radiation, which also leads to the SIF-NIRvR gap. We should note that although many studies have reported on the linearity of SIF and NIRvR at monthly timescales and coarse spatial resolutions, for NIRvR to be a reliable proxy of SIF, Φ_F would need to remain constant. Nevertheless, all evidence indicates that SIF and NIRvR could be complementary, and we confirm that in the alpine grasslands of the Tibetan Plateau, NIRvR is a reliable proxy on EOS for satellite-retrieved SIF at an 8-day temporal scale.

Moreover, to test whether TROPOMI NDVI (especially Red reflectance) without atmospheric correction causes a significant bias in NIRvR results, we further compared the seasonal dynamics and phenology of two NIRvRs at the site and regional scales. NIRvR was calculated using NDVI from MCD43A4 SR and TROPOMI TOA datasets, respectively, keeping the NIR radiance all from the TROPOMI sensor. Note that the MCD43A4-based NDVI is atmospherically corrected, while the NDVI of TROPOMI is not. The results of NIRvRs based on TROPOMI and MCD43A4 consistently show that the absence of atmospheric correction has a greater impact on the difference in NIRvR magnitude than on the difference in the seasonality (phenology) (Fig. S58-S60). Using the MCD43A4-based NIRvR leads to higher NIRvR values, but makes SOS earlier and EOS later, apparently not as close to SIF as the TROPOMI-based NIRvR. Setting aside the differences related to signal quality among sensors, the NIRvR discrepancies between TROPOMI and MCD43A4 are most likely because the two satellite sensors use different bandwidths to calculate NDVI (Guanter et al., 2021) and have differences in sun-sensor geometry (Dechant et al., 2022). A previous study found that TROPOMI-based NIRv (NDVI × NIR reflectance) outperformed MODIS-based NIRv. They also found that NIRvR from TROPOMI NIR radiance showed a higher spatial and temporal correlation to SIF than NIRvR from MODIS (Dechant et al., 2022). These results are in agreement with our findings. Overall, atmospheric corrections do not appear to have a significant impact on the NIRvR-retrieved phenological

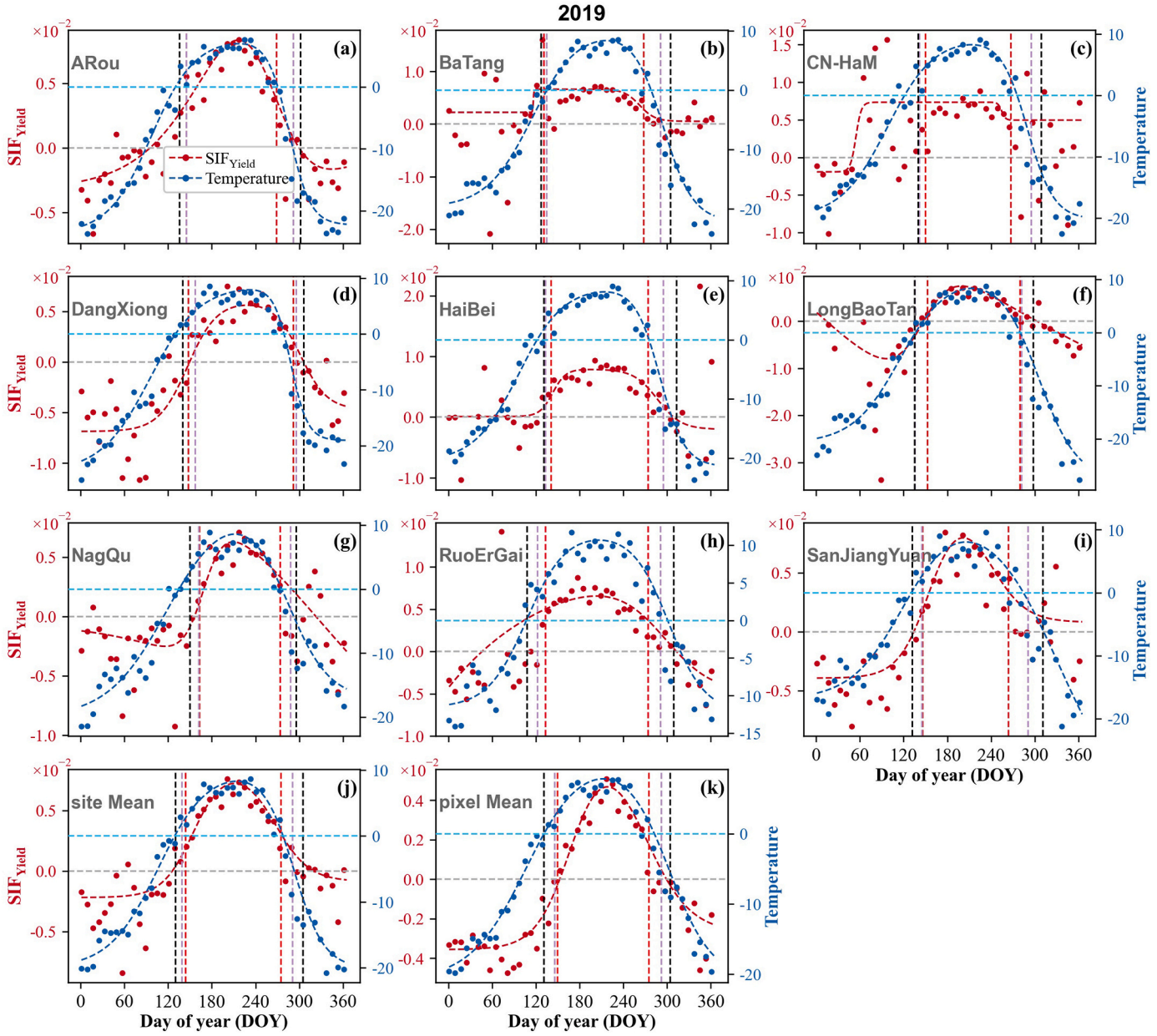

Fig. 10. The seasonal dynamics of the site-averaged and region-averaged fluorescence yield (SIF_{Yield}) and night-time mean air temperature in the year 2019. The red, purple, and black vertical lines are SOS and EOS estimated from TROPOMI SIF, TROPOMI NDVI, and MCD43 NDVI, respectively. The blue horizontal dashed line depicts a temperature of 0 °C, while the gray horizontal dashed line represents a SIF_{Yield} of 0. SIF_{Yield} is unitless. (For interpretation of the references to colour in this figure legend, the reader is referred to the web version of this article.)

transition dates, and more importantly, keep the NDVI and NIR radiance from the same sensor so that potential geometric correction, spatial resolution and band windows mismatches between SIF and NIRvR can be minimized. Our result indicates that it is a good practice to use SIF and NIRvR acquired from the same satellite sensor with the same sun-sensor geometry. This study is the first to evaluate the phenological characterization of NIRvR at the pixel scale, though there have been several studies to look at SIF-NIRvR space-time relationships. In fact, only NIRvR is comparable with SIF because they have the same unit, while reflectance-based VIs and radiance-based SIF with different units are not directly comparable before their normalization by SIF / PAR or VIs × PAR. More direct comparisons between SIF and NIRvR and NIRvR-relevant studies on phenological characterization and sensitivity are needed across vegetation types and spatial-temporal scales.

Although the VIs datasets exhibit large uncertainties in EOS estimations, we need to note that, indeed, matching the two VIs- and SIF-retrieved phenology is still challenging. Given that VIs have long-time records of satellite observations with high signal quality and high spatiotemporal resolution (Badgley et al., 2017), further studies are needed to develop better VIs-specific phenology extraction algorithms to eliminate the influence of soil background. And similarly, a composite indicator, like NIRvR, coupled with vegetation indices should be further tested and applied. We call for the integration and sharing of in-situ canopy-level SIF, phenoCam, EC flux tower, and surface reflectance data across the Tibetan Plateau and broader region, as well as the development of more robust algorithms that will refine our determination of phenological timings at the landscape level. Meanwhile, SIF can be used to estimate GPP and its seasonality, therefore, very high-quality and high-resolution SIF products to determine phenological metrics should not be ignored. Here, the SIF soundings from TROPOMI were

aggregated within each 0.2° grid cell with robust quality control of the data, although there may still be a small amount of SIF retrievals with high uncertainties (Fig. S3), suggesting that the ultimate SIF products should avoid the need for aggregation to coarser scales in terms of sounding footprints, viewing geometry, and signal quality (Ryu et al., 2019; Dechant et al., 2022). Future spaceborne missions with finer spatial and temporal resolutions, including the upcoming FLuorescence EXplorer (FLEX) onboard the Sentinel-3 satellite and the Geostationary Carbon Cycle Observatory (GeoCARB) (Drusch et al., 2017; Polonsky et al., 2014), should be utilized to further improve our understanding of vegetation phenology at the global scale.

5. Conclusions

In this study, we utilized the state-of-the-art TROPOMI SIF data with high spatial and temporal resolutions to compare the SIF-based phenological metrics against vegetation indices-based ones at sites and pixel scales from 2019 to 2021 in the Tibetan Plateau. Our results show the systemic inconsistency in phenological metrics between the SIF and VIs. Specifically, the LGS derived from the NDVI, EVI, and NIRv is more than two months longer than the one from SIF and GPP, which is mainly determined by the later EOS. Furthermore, we confirm that TROPOMI SIF can match well with GPP in tracking the seasonal variances of alpine grasslands that revealing satellite-derived TROPOMI SIF and GPP can synergistically characterize the seasonality of photosynthesis. Furthermore, air temperature analysis at the time when SOS/EOS occurs shows that SIF-based SOS and EOS dates occur after air temperatures exceed the freezing point, but greenness-based SOS and EOS dates occur even air temperature is already below zero. These results revealed that VIs with most phenology extraction methods has a large uncertainty in terms of biology, and thus our study highlights the need to re-evaluate the current SOS and EOS data products derived from the vegetation indices and develop new SOS and EOS data products from optical satellite sensors. It is necessary to utilize physiology-based SIF to constrain the terrestrial ecosystem model in addition to the traditional canopy structure-related indicators.

CRediT authorship contribution statement

Jilin Yang: Conceptualization, Methodology, Validation, Writing – original draft, Writing – review & editing, Formal analysis, Visualization. **Xiangming Xiao:** Conceptualization, Methodology, Writing – original draft, Formal analysis, Visualization, Writing – review & editing, Supervision, Project administration, Funding acquisition. **Russell Doughty:** Conceptualization, Methodology, Data curation, Resources, Validation, Writing – original draft. **Miaomiao Zhao:** Conceptualization, Methodology, Validation, Writing – original draft, Writing – review & editing, Formal analysis, Visualization. **Yao Zhang:** Conceptualization, Methodology, Writing – original draft, Writing – review & editing. **Philipp Köhler:** Methodology, Resources, Writing – original draft, Data curation. **Xiaocui Wu:** Methodology, Writing – original draft, Resources, Data curation. **Christian Frankenberg:** Methodology, Resources, Writing – original draft. **Jinwei Dong:** Conceptualization, Funding acquisition, Investigation, Project administration, Supervision, Writing – original draft, Writing – review & editing.

Declaration of Competing Interest

The authors declare that they have no known competing financial interests or personal relationships that could have appeared to influence the work reported in this paper.

Data availability

Data will be made available on request.

Acknowledgments

This research was funded by the National Key Research and Development Program of China (2018YFA0606100), the Strategic Priority Research Program (XDA26010202), the Key Research Program of Frontier Sciences (QYZDB-SSW-DQC005) of the Chinese Academy of Sciences (CAS), and the U.S. National Science Foundation (1911955). We acknowledge all contributors of the ChinaFlux (www.chinaflux.org) and FLUXNET Network (http://fluxnet.fluxdata.org/). We thank the MODIS Science Team for generating and sharing a variety of MODIS data (https://e4ftl01.cr.usgs.gov). The authors are grateful to the Climate Data Store for sharing the ERA5 climate dataset (https://cds.climate.copernicus.eu). The TROPOSIF products were generated by the TROPOSIF team conducted by NOVELTIS under the European Space Agency (ESA) Sentinel-5p + Innovation activity Contract (No 4000127461/19/I-NS). J. Y. also gratefully acknowledges the China Scholarship Council for the financial support of a 24-month study at the University of Oklahoma.

Appendix A. Supplementary data

Supplementary data to this article can be found online at https://doi.org/10.1016/j.rse.2022.113209.

References

Aber, J.D., Reich, P.B., Goulden, M.L., 1996. Extrapolating leaf CO_2 exchange to the canopy: a generalized model of forest photosynthesis compared with measurements by eddy correlation. Oecologia 106, 257–265.
Adole, T., Dash, J., Rodriguez-Galiano, V., Atkinson, P.M., 2019. Photoperiod controls vegetation phenology across Africa. Commun Biol 2, 391.
Anav, A., Friedlingstein, P., Beer, C., Ciais, P., Harper, A., Jones, C., Murray-Tortarolo, G., Papale, D., Parazoo, N.C., Peylin, P., Piao, S., Sitch, S., Viovy, N., Wiltshire, A., Zhao, M., 2015. Spatiotemporal patterns of terrestrial gross primary production: a review. Rev. Geophys. 53, 785–818.
Badgley, G., Field, C.B., Berry, J.A., 2017. Canopy near-infrared reflectance and terrestrial photosynthesis. Sci. Adv. 3, e1602244.
Baldocchi, D.D., Ryu, Y., Dechant, B., Eichelmann, E., Hemes, K., Ma, S., Sanchez, C.R., Shortt, R., Szutu, D., Valach, A., Verfaillie, J., Badgley, G., Zeng, Y., Berry, J.A., 2020. Outgoing near-infrared radiation from vegetation scales with canopy photosynthesis across a Spectrum of function, structure, physiological capacity, and weather. J. Geophys. Res. Biogeosci. 125.
Chang, Q., Xiao, X., Jiao, W., Wu, X., Doughty, R., Wang, J., Du, L., Zou, Z., Qin, Y., 2019. Assessing consistency of spring phenology of snow-covered forests as estimated by vegetation indices, gross primary production, and solar-induced chlorophyll fluorescence. Agric. For. Meteorol. 275, 305–316.
Chen, J., Jönsson, P., Tamura, M., Gu, Z., Matsushita, B., Eklundh, L., 2004. A simple method for reconstructing a high-quality NDVI time-series data set based on the Savitzky–Golay filter. Remote Sens. Environ. 91, 332–344.
Chen, H., Zhu, Q., Peng, C., Wu, N., Wang, Y., Fang, X., Gao, Y., Zhu, D., Yang, G., Tian, J., Kang, X., Piao, S., Ouyang, H., Xiang, W., Luo, Z., Jiang, H., Song, X., Zhang, Y., Yu, G., Zhao, X., Gong, P., Yao, T., Wu, J., 2013. The impacts of climate change and human activities on biogeochemical cycles on the Qinghai-Tibetan plateau. Glob. Chang. Biol. 19, 2940–2955.
Chen, X., An, S., Inouye, D.W., Schwartz, M.D., 2015. Temperature and snowfall trigger alpine vegetation green-up on the world's roof. Glob. Chang. Biol. 21, 3635–3646.
Cong, N., Shen, M., Piao, S., Chen, X., An, S., Yang, W., Fu, Y.H., Meng, F., Wang, T., 2017. Little change in heat requirement for vegetation green-up on the Tibetan plateau over the warming period of 1998–2012. Agric. For. Meteorol. 232, 650–658.
Dechant, B., Ryu, Y., Badgley, G., Zeng, Y., Berry, J.A., Zhang, Y., Goulas, Y., Li, Z., Zhang, Q., Kang, M., Li, J., Moya, I., 2020. Canopy structure explains the relationship between photosynthesis and sun-induced chlorophyll fluorescence in crops. Remote Sens. Environ. 241.
Dechant, B., Ryu, Y., Badgley, G., Köhler, P., Rascher, U., Migliavacca, M., Zhang, Y., Tagliabue, G., Guan, K., Rossini, M., Goulas, Y., Zeng, Y., Frankenberg, C., Berry, J. A., 2022. NIRVP: a robust structural proxy for sun-induced chlorophyll fluorescence and photosynthesis across scales. Remote Sens. Environ. 268.
Doughty, R., Kohler, P., Frankenberg, C., Magney, T.S., Xiao, X., Qin, Y., Wu, X., Moore 3rd, B., 2019. TROPOMI reveals dry-season increase of solar-induced chlorophyll fluorescence in the Amazon forest. Proc. Natl. Acad. Sci. U. S. A. 116, 22393–22398.
Doughty, R., Xiao, X., Köhler, P., Frankenberg, C., Qin, Y., Wu, X., Ma, S., Moore, B., 2021a. Global-scale consistency of Spaceborne vegetation indices, chlorophyll fluorescence, and photosynthesis. J. Geophys. Res. Biogeosci. 126.
Doughty, R., Xiao, X., Qin, Y., Wu, X., Zhang, Y., Moore, B., 2021b. Small anomalies in dry-season greenness and chlorophyll fluorescence for Amazon moist tropical forests during El Niño and La Niña. Remote Sens. Environ. 253, 112196.

Drusch, M., Moreno, J., Bello, U.D., Franco, R., Goulas, Y., Huth, A., Kraft, S., Middleton, E.M., Miglietta, F., Mohammed, G., Nedbal, L., Rascher, U., Schüttemeyer, D., Verhoef, W., 2017. The FLuorescence EXplorer Mission concept—ESA's earth Explorer 8. IEEE Trans. Geosci. Remote Sens. 55, 1273–1284.
Ensminger, I., Schmidt, L., Lloyd, J., 2008. Soil temperature and intermittent frost modulate the rate of recovery of photosynthesis in scots pine under simulated spring conditions. New Phytol. 177, 428–442.
Frankenberg, C., O'Dell, C., Guanter, L., McDuffie, J., 2012. Remote sensing of near-infrared chlorophyll fluorescence from space in scattering atmospheres: implications for its retrieval and interferences with atmospheric CO₂ retrievals. Atmosph. Measur. Tech. 5, 2081–2094.
Friedl, M., Sulla-Menashe, D., 2015. MCD12C1 MODIS/Terra+aqua land cover type yearly L3 global 0.05Deg CMG V006. In: NASA EOSDIS Land Processes DAAC.
Friedl, M., Gray, J., Sulla-Menashe, D., 2019. MCD12Q2 MODIS/Terra+ Aqua Land Cover Dynamics Yearly L3 Global 500m SIN Grid V006. NASA EOSDIS Land Processes DAAC. NASA, Washington, DC, USA.
Garrity, S.R., Bohrer, G., Maurer, K.D., Mueller, K.L., Vogel, C.S., Curtis, P.S., 2011. A comparison of multiple phenology data sources for estimating seasonal transitions in deciduous forest carbon exchange. Agric. For. Meteorol. 151, 1741–1752.
Gonsamo, A., Chen, J.M., D'Odorico, P., 2013. Deriving land surface phenology indicators from CO2 eddy covariance measurements. Ecol. Indic. 29, 203–207.
Guanter, L., Zhang, Y., Jung, M., Joiner, J., Voigt, M., Berry, J.A., Frankenberg, C., Huete, A.R., Zarco-Tejada, P., Lee, J.E., Moran, M.S., Ponce-Campos, G., Beer, C., Camps-Valls, G., Buchmann, N., Gianelle, D., Klumpp, K., Cescatti, A., Baker, J.M., Griffis, T.J., 2014. Global and time-resolved monitoring of crop photosynthesis with chlorophyll fluorescence. Proc. Natl. Acad. Sci. U. S. A. 111, E1327–E1333.
Guanter, L., Aben, I., Tol, P., Krijger, J.M., Hollstein, A., Köhler, P., Damm, A., Joiner, J., Frankenberg, C., Landgraf, J., 2015. Potential of the TROPOspheric monitoring instrument (TROPOMI) onboard the Sentinel-5 precursor for the monitoring of terrestrial chlorophyll fluorescence. Atmosph. Measur. Tech. 8, 1337–1352.
Guanter, L., Bacour, C., Schneider, A., Aben, I., van Kempen, T.A., Maignan, F., Retscher, C., Köhler, P., Frankenberg, C., Joiner, J., Zhang, Y., 2021. The TROPOSIF global sun-induced fluorescence dataset from the sentinel-5P TROPOMI mission. Earth System Sci. Data 13, 5423–5440.
Hersbach, H., Bell, B., Berrisford, P., Hirahara, S., Horányi, A., Muñoz-Sabater, J., Nicolas, J., Peubey, C., Radu, R., Schepers, D., 2020. The ERA5 global reanalysis. Q. J. R. Meteorol. Soc. 146, 1999–2049.
Huang, K., Zhang, Y., Tagesson, T., Brandt, M., Wang, L., Chen, N., Zu, J., Jin, H., Cai, Z., Tong, X., Cong, N., Fensholt, R., 2021. The confounding effect of snow cover on assessing spring phenology from space: a new look at trends on the Tibetan plateau. Sci. Total Environ. 756, 144011.
Huete, A., Didan, K., Miura, T., Rodriguez, E.P., Gao, X., Ferreira, L.G., 2002. Overview of the radiometric and biophysical performance of the MODIS vegetation indices. Remote Sens. Environ. 83, 195–213.
Jeong, S.-J., Schimel, D., Frankenberg, C., Drewry, D.T., Fisher, J.B., Verma, M., Berry, J. A., Lee, J.-E., Joiner, J., 2017. Application of satellite solar-induced chlorophyll fluorescence to understanding large-scale variations in vegetation phenology and function over northern high latitude forests. Remote Sens. Environ. 190, 178–187.
Jin, H., Eklundh, L., 2014. A physically based vegetation index for improved monitoring of plant phenology. Remote Sens. Environ. *152*, 512–525.
Joiner, J., Guanter, L., Lindstrot, R., Voigt, M., Vasilkov, A.P., Middleton, E.M., Huemmrich, K.F., Yoshida, Y., Frankenberg, C., 2013. Global monitoring of terrestrial chlorophyll fluorescence from moderate-spectral-resolution near-infrared satellite measurements: methodology, simulations, and application to GOME-2. Atmosph. Measur. Tech. 6, 2803–2823.
Joiner, J., Yoshida, Y., Vasilkov, A.P., Schaefer, K., Jung, M., Guanter, L., Zhang, Y., Garrity, S., Middleton, E.M., Huemmrich, K.F., Gu, L., Belelli Marchesini, L., 2014. The seasonal cycle of satellite chlorophyll fluorescence observations and its relationship to vegetation phenology and ecosystem atmosphere carbon exchange. Remote Sens. Environ. 152, 375–391.
Keenan, T.F., Gray, J., Friedl, M.A., Toomey, M., Bohrer, G., Hollinger, D.Y., Munger, J. W., O'Keefe, J., Schmid, H.P., Wing, I.S., Yang, B., Richardson, A.D., 2014. Net carbon uptake has increased through warming-induced changes in temperate forest phenology. Nat. Clim. Chang. 4, 598–604.
Köhler, P., Frankenberg, C., Magney, T.S., Guanter, L., Joiner, J., Landgraf, J., 2018. Global retrievals of solar induced chlorophyll fluorescence with TROPOMI: first results and inter-sensor comparison to OCO-2. Geophys. Res. Lett. 45, 10456–10463.
Lekner, J., Dorf, M.C., 1988. Why some things are darker when wet. Appl. Opt. 27, 1278–1280.
Li, X., Xiao, J., He, B., Altaf Arain, M., Beringer, J., Desai, A.R., Emmel, C., Hollinger, D. Y., Krasnova, A., Mammarella, I., Noe, S.M., Ortiz, P.S., Rey-Sanchez, A.C., Rocha, A. V., Varlagin, A., 2018. Solar-induced chlorophyll fluorescence is strongly correlated with terrestrial photosynthesis for a wide variety of biomes: first global analysis based on OCO-2 and flux tower observations. Glob. Chang. Biol. 24, 3990–4008.
Lu, X., Liu, Z., Zhou, Y., Liu, Y., An, S., Tang, J., 2018. Comparison of phenology estimated from reflectance-based indices and solar-induced chlorophyll fluorescence (SIF) observations in a temperate Forest using GPP-based phenology as the standard. Remote Sens. 10.
Magney, T.S., Bowling, D.R., Logan, B.A., Grossmann, K., Stutz, J., Blanken, P.D., Burns, S.P., Cheng, R., Garcia, M.A., Khler, P., Lopez, S., Parazoo, N.C., Raczka, B., Schimel, D., Frankenberg, C., 2019. Mechanistic evidence for tracking the seasonality of photosynthesis with solar-induced fluorescence. Proc. Natl. Acad. Sci. U. S. A. 116, 11640–11645.
Magney, T.S., Barnes, M.L., Yang, X., 2020. On the covariation of chlorophyll fluorescence and photosynthesis across scales. Geophys. Res. Lett. 47.
McGuire, A.D., Melillo, J.M., Joyce, L.A., Kicklighter, D.W., Schloss, A.L., 1992. Interactions between carbon and nitrogen dynamics in estimating net primary productivity for potential vegetation in North America. Glob. Biogeochem. Cycles 6, 101–124.
Melaas, E.K., Sulla-Menashe, D., Gray, J.M., Black, T.A., Morin, T.H., Richardson, A.D., Friedl, M.A., 2016. Multisite analysis of land surface phenology in north American temperate and boreal deciduous forests from Landsat. Remote Sens. Environ. 186, 452–464.
Nagler, P.L., Daughtry, C.S.T., Goward, S.N., 2000. Plant litter and soil reflectance. Remote Sens. Environ. 71, 207–215.
Noormets, A., 2009. Phenology of Ecosystem Processes: Applications in Global Change Research. Springer.
NOVELTIS, UPV, SRON, LSCE, & ESA, 2021. The TROPOSIF Global Sun-Induced Fluorescence Dataset from the TROPOMI Mission. https://doi.org/10.5270/esa-s5p_innovation-sif-20180501_20210320-v2.1-202104.
Piao, S., Liu, Q., Chen, A., Janssens, I.A., Fu, Y., Dai, J., Liu, L., Lian, X., Shen, M., Zhu, X., 2019. Plant phenology and global climate change: current progresses and challenges. Glob. Chang. Biol. 25, 1922–1940.
Pierrat, Z., Magney, T., Parazoo, N.C., Grossmann, K., Bowling, D.R., Seibt, U., Johnson, B., Helgason, W., Barr, A., Bortnik, J., Norton, A., Maguire, A., Frankenberg, C., Stutz, J., 2022. Diurnal and seasonal dynamics of solar-induced chlorophyll fluorescence, vegetation indices, and gross primary productivity in the boreal Forest. Journal of geophysical research. Biogeosciences 127.
Polonsky, I.N., O'Brien, D.M., Kumer, J.B., O'Dell, C.W., the geo, C.T, 2014. Performance of a geostationary mission, geoCARB, to measure CO_2, CH_4 and CO column-averaged concentrations. Atmos. Meas. Tech. 7, 959–981.
Raich, J.W., Rastetter, E.B., Melillo, J.M., Kicklighter, D.W., Steudler, P.A., Peterson, B. J., Grace, A.L., Moore III, B., Vorosmarty, C.J., 1991. Potential net primary productivity in South America: application of a global model. Ecol. Appl. 1 (4), 399–429.
Richardson, A.D., Anderson, R.S., Arain, M.A., Barr, A.G., Bohrer, G., Chen, G., Chen, J. M., Ciais, P., Davis, K.J., Desai, A.R., Dietze, M.C., Dragoni, D., Garrity, S.R., Gough, C.M., Grant, R., Hollinger, D.Y., Margolis, H.A., McCaughey, H., Migliavacca, M., Monson, R.K., Munger, J.W., Poulter, B., Raczka, B.M., Ricciuto, D. M., Sahoo, A.K., Schaefer, K., Tian, H., Vargas, R., Verbeeck, H., Xiao, J., Xue, Y., 2012. Terrestrial biosphere models need better representation of vegetation phenology: results from the north American carbon program site synthesis. Glob. Chang. Biol. 18, 566–584.
Richardson, A.D., Keenan, T.F., Migliavacca, M., Ryu, Y., Sonnentag, O., Toomey, M., 2013. Climate change, phenology, and phenological control of vegetation feedbacks to the climate system. Agric. For. Meteorol. 169, 156–173.
Riggs, G.A., Hall, D.K., Román, M.O., 2017. Overview of NASA's MODIS and visible infrared imaging radiometer suite (VIIRS) snow-cover earth system data records. Earth Syst. Sci. Data 9, 765–777.
Ryu, Y., Berry, J.A., Baldocchi, D.D., 2019. What is global photosynthesis? History, uncertainties and opportunities. Remote Sens. Environ. 223, 95–114.
Schaaf, C., Wang, Z., 2015a. MCD43A2 MODIS/Terra+aqua BRDF/albedo quality daily L3 global - 500m V006. In: NASA EOSDIS Land Processes DAAC. https://doi.org/10.5067/MODIS/MCD43A2.006.
Schaaf, C., Wang, Z., 2015b. MCD43A4 MODIS/Terra+aqua BRDF/albedo nadir BRDF adjusted ref daily L3 global - 500m V006. In: NASA EOSDIS Land Processes DAAC. https://doi.org/10.5067/MODIS/MCD43A4.006.
Shen, M., Sun, Z., Wang, S., Zhang, G., Kong, W., Chen, A., Piao, S., 2013. No evidence of continuously advanced green-up dates in the Tibetan plateau over the last decade. Proc. Natl. Acad. Sci. U. S. A. 110, E2329.
Shen, M., Piao, S., Cong, N., Zhang, G., Jassens, I.A., 2015a. Precipitation impacts on vegetation spring phenology on the Tibetan Plateau. Glob. Chang. Biol. 21, 3647–3656.
Shen, M., Piao, S., Dorji, T., Liu, Q., Cong, N., Chen, X., An, S., Wang, S., Wang, T., Zhang, G., 2015b. Plant phenological responses to climate change on the Tibetan plateau: research status and challenges. Natl. Sci. Rev. 2, 454–467.
Shen, M., Piao, S., Chen, X., An, S., Fu, Y.H., Wang, S., Cong, N., Janssens, I.A., 2016. Strong impacts of daily minimum temperature on the green-up date and summer greenness of the Tibetan Plateau. Glob. Chang. Biol. 22, 3057–3066.
Smith, W.K., Dannenberg, M.P., Yan, D., Herrmann, S., Barnes, M.L., Barron-Gafford, G. A., Biederman, J.A., Ferrenberg, S., Fox, A.M., Hudson, A., Knowles, J.F., MacBean, N., Moore, D.J.P., Nagler, P.L., Reed, S.C., Rutherford, W.A., Scott, R.L., Wang, X., Yang, J., 2019. Remote sensing of dryland ecosystem structure and function: Progress, challenges, and opportunities. Remote Sens. Environ. 233, 111401.
Song, L., Guanter, L., Guan, K., You, L., Huete, A., Ju, W., Zhang, Y., 2018. Satellite sun-induced chlorophyll fluorescence detects early response of winter wheat to heat stress in the Indian indo-Gangetic Plains. Glob. Chang. Biol. 24, 4023–4037.
Sun, Y., Fu, R., Dickinson, R., Joiner, J., Frankenberg, C., Gu, L., Xia, Y., Fernando, N., 2015. Drought onset mechanisms revealed by satellite solar-induced chlorophyll fluorescence: insights from two contrasting extreme events. J. Geophys. Res. Biogeosci. 120, 2427–2440.
Sun, Y., Frankenberg, C., Wood, J.D., Schimel, D.S., Jung, M., Guanter, L., Drewry, D.T., Verma, M., Porcar-Castell, A., Griffis, T.J., Gu, L., Magney, T.S., Kohler, P., Evans, B., Yuen, K., 2017. OCO-2 advances photosynthesis observation from space via solar-induced chlorophyll fluorescence. Science 358.
Sun, Y., Frankenberg, C., Jung, M., Joiner, J., Guanter, L., Köhler, P., Magney, T., 2018. Overview of solar-induced chlorophyll fluorescence (SIF) from the orbiting carbon Observatory-2: retrieval, cross-mission comparison, and global monitoring for GPP. Remote Sens. Environ. 209, 808–823.

Tian, J., Philpot, W.D., 2015. Relating water absorption features to soil moisture characteristics. Imag. Spectr. *xx* 9611.
Tucker, C.J., 1979. Red and photographic infrared linear combinations for monitoring vegetation. Remote Sens. Environ. 8, 127–150.
Turner, A.J., Köhler, P., Magney, T.S., Frankenberg, C., Fung, I., Cohen, R.C., 2020. A double peak in the seasonality of California's photosynthesis as observed from space. Biogeosciences 17, 405–422.
van der Tol, C., Vilfan, N., Dauwe, D., Cendrero-Mateo, M.P., Yang, P., 2019. The scattering and re-absorption of red and near-infrared chlorophyll fluorescence in the models Fluspect and SCOPE. Remote Sens. Environ. 232.
Veefkind, J.P., Aben, I., McMullan, K., Förster, H., de Vries, J., Otter, G., Claas, J., Eskes, H.J., de Haan, J.F., Kleipool, Q., van Weele, M., Hasekamp, O., Hoogeveen, R., Landgraf, J., Snel, R., Tol, P., Ingmann, P., Voors, R., Kruizinga, B., Vink, R., Visser, H., Levelt, P.F., 2012. TROPOMI on the ESA Sentinel-5 precursor: a GMES mission for global observations of the atmospheric composition for climate, air quality and ozone layer applications. Remote Sens. Environ. 120, 70–83.
Vermote, E., 2015. MOD09A1 MODIS/Terra surface reflectance 8-day L3 global 500m SIN grid V006. In: NASA EOSDIS Land Processes DAAC. https://doi.org/10.5067/MODIS/MOD09A1.006.
Walther, S., Voigt, M., Thum, T., Gonsamo, A., Zhang, Y., Kohler, P., Jung, M., Varlagin, A., Guanter, L., 2016. Satellite chlorophyll fluorescence measurements reveal large-scale decoupling of photosynthesis and greenness dynamics in boreal evergreen forests. Glob. Chang. Biol. 22, 2979–2996.
Walther, S., Duveiller, G., Jung, M., Guanter, L., Cescatti, A., Camps-Valls, G., 2019. Satellite observations of the contrasting response of trees and grasses to variations in water availability. Geophys. Res. Lett. 46, 1429–1440.
Wang, T., Peng, S., Lin, X., Chang, J., 2013. Declining snow cover may affect spring phenological trend on the Tibetan plateau. Proc. Natl. Acad. Sci. U. S. A. 110, E2854–E2855.
Wang, C., Beringer, J., Hutley, L.B., Cleverly, J., Li, J., Liu, Q., Sun, Y., 2019. Phenology dynamics of dryland ecosystems along the north Australian tropical transect revealed by satellite solar-induced chlorophyll fluorescence. Geophys. Res. Lett. 46, 5294–5302.
Wang, C., Guan, K., Peng, B., Chen, M., Jiang, C., Zeng, Y., Wu, G., Wang, S., Wu, J., Yang, X., Frankenberg, C., Köhler, P., Berry, J., Bernacchi, C., Zhu, K., Alden, C., Miao, G., 2020a. Satellite footprint data from OCO-2 and TROPOMI reveal significant spatio-temporal and inter-vegetation type variabilities of solar-induced fluorescence yield in the U.S Midwest. Remote Sens. Environ. 241.
Wang, F., Chen, B., Lin, X., Zhang, H., 2020b. Solar-induced chlorophyll fluorescence as an indicator for determining the end date of the vegetation growing season. Ecol. Indic. 109.
Wang, X., Dannenberg, M.P., Yan, D., Jones, M.O., Kimball, J.S., Moore, D.J.P., Leeuwen, W.J.D., Didan, K., Smith, W.K., 2020c. Globally consistent patterns of asynchrony in vegetation phenology derived from optical, microwave, and fluorescence satellite data. J. Geophys. Res. Biogeosci. 125 e2020JG005732.
Wen, J., Köhler, P., Duveiller, G., Parazoo, N.C., Magney, T.S., Hooker, G., Yu, L., Chang, C.Y., Sun, Y., 2020. A framework for harmonizing multiple satellite instruments to generate a long-term global high spatial-resolution solar-induced chlorophyll fluorescence (SIF). Remote Sens. Environ. 239, 111644.
Wu, C., Chen, J.M., Black, T.A., Price, D.T., Kurz, W.A., Desai, A.R., Gonsamo, A., Jassal, R.S., Gough, C.M., Bohrer, G., Dragoni, D., Herbst, M., Gielen, B., Berninger, F., Vesala, T., Mammarella, I., Pilegaard, K., Blanken, P.D., 2013. Interannual variability of net ecosystem productivity in forests is explained by carbon flux phenology in autumn. Glob. Ecol. Biogeogr. 22, 994–1006.
Wu, C., Gonsamo, A., Gough, C.M., Chen, J.M., Xu, S., 2014. Modeling growing season phenology in north American forests using seasonal mean vegetation indices from MODIS. Remote Sens. Environ. 147, 79–88.
Wu, C., Wang, X., Wang, H., Ciais, P., Peñuelas, J., Myneni, R.B., Desai, A.R., Gough, C. M., Gonsamo, A., Black, A.T., Jassal, R.S., Ju, W., Yuan, W., Fu, Y., Shen, M., Li, S., Liu, R., Chen, J.M., Ge, Q., 2018a. Contrasting responses of autumn-leaf senescence to daytime and night-time warming. Nat. Clim. Chang. 8, 1092–1096.
Wu, X., Xiao, X., Zhang, Y., He, W., Wolf, S., Chen, J., He, M., Gough, C.M., Qin, Y., Zhou, Y., Doughty, R., Blanken, P.D., 2018b. Spatiotemporal consistency of four gross primary production products and solar-induced chlorophyll fluorescence in response to climate extremes across CONUS in 2012. J. Geophys. Res. Biogeosci. 123, 3140–3161.
Wu, G., Guan, K., Jiang, C., Peng, B., Kimm, H., Chen, M., Yang, X., Wang, S., Suyker, A. E., Bernacchi, C.J., Moore, C.E., Zeng, Y., Berry, J.A., Cendrero-Mateo, M.P., 2020. Radiance-based NIRv as a proxy for GPP of corn and soybean. Environ. Res. Lett. 15.
Xia, J., Niu, S., Ciais, P., Janssens, I.A., Chen, J., Ammann, C., Arain, A., Blanken, P.D., Cescatti, A., Bonal, D., Buchmann, N., Curtis, P.S., Chen, S., Dong, J., Flanagan, L.B., Frankenberg, C., Georgiadis, T., Gough, C.M., Hui, D., Kiely, G., Li, J., Lund, M., Magliulo, V., Marcolla, B., Merbold, L., Montagnani, L., Moors, E.J., Olesen, J.E., Piao, S., Raschi, A., Roupsard, O., Suyker, A.E., Urbaniak, M., Vaccari, F.P., Varlagin, A., Vesala, T., Wilkinson, M., Weng, E., Wohlfahrt, G., Yan, L., Luo, Y., 2015. Joint control of terrestrial gross primary productivity by plant phenology and physiology. Proc. Natl. Acad. Sci. U. S. A. 112, 2788–2793.
Xiao, X., 2004. Modeling gross primary production of temperate deciduous broadleaf forest using satellite images and climate data. Remote Sens. Environ. 91, 256–270.
Xiao, X., Boles, S., Frolking, S., Salas, W., Moore, B., Li, C., He, L., Zhao, R., 2002. Observation of flooding and rice transplanting of paddy rice fields at the site to landscape scales in China using VEGETATION sensor data. Int. J. Remote Sens. 23, 3009–3022.
Xiao, X., Hollinger, D., Aber, J., Goltz, M., Davidson, E.A., Zhang, Q., Moore, B., 2004. Satellite-based modeling of gross primary production in an evergreen needleleaf forest. Remote Sens. Environ. 89, 519–534.
Xiao, J., Li, X., He, B., Arain, M.A., Beringer, J., Desai, A.R., Emmel, C., Hollinger, D.Y., Krasnova, A., Mammarella, I., Noe, S.M., Serrano Ortiz, P., Rey-Sanchez, C., Rocha, A.V., Varlagin, A., 2019. Solar-induced chlorophyll fluorescence exhibits a universal relationship with gross primary productivity across a wide variety of biomes. Glob. Chang. Biol. 25, e4–e6.
Yang, X., Tang, J., Mustard, J.F., Lee, J.-E., Rossini, M., Joiner, J., Munger, J.W., Kornfeld, A., Richardson, A.D., 2015. Solar-induced chlorophyll fluorescence that correlates with canopy photosynthesis on diurnal and seasonal scales in a temperate deciduous forest. Geophys. Res. Lett. 42, 2977–2987.
Yang, J., Dong, J., Xiao, X., Dai, J., Wu, C., Xia, J., Zhao, G., Zhao, M., Li, Z., Zhang, Y., Ge, Q., 2019. Divergent shifts in peak photosynthesis timing of temperate and alpine grasslands in China. Remote Sens. Environ. 233.
Yin, Y., Byrne, B., Liu, J., Wennberg, P.O., Davis, K.J., Magney, T., Köhler, P., He, L., Jeyaram, R., Humphrey, V., Gerken, T., Feng, S., Digangi, J.P., Frankenberg, C., 2020. Cropland carbon uptake delayed and reduced by 2019 Midwest floods. AGU Adv. 1.
Yu, H., Luedeling, E., Xu, J., 2010. Winter and spring warming result in delayed spring phenology on the Tibetan plateau. Proc. Natl. Acad. Sci. U. S. A. 107, 22151–22156.
Zeng, Y., Badgley, G., Dechant, B., Ryu, Y., Chen, M., Berry, J.A., 2019. A practical approach for estimating the escape ratio of near-infrared solar-induced chlorophyll fluorescence. Remote Sens. Environ. 232.
Zeng, Y., Chen, M., Hao, D., Damm, A., Badgley, G., Rascher, U., Johnson, J.E., Dechant, B., Siegmann, B., Ryu, Y., Qiu, H., Krieger, V., Panigada, C., Celesti, M., Miglietta, F., Yang, X., Berry, J.A., 2022a. Combining near-infrared radiance of vegetation and fluorescence spectroscopy to detect effects of abiotic changes and stresses. Remote Sens. Environ. 270.
Zeng, Y., Hao, D., Huete, A., Dechant, B., Berry, J., Chen, J.M., Joiner, J., Frankenberg, C., Bond-Lamberty, B., Ryu, Y., Xiao, J., Asrar, G.R., Chen, M., 2022b. Optical vegetation indices for monitoring terrestrial ecosystems globally. Nat. Rev. Earth Environ. 3, 477–493.
Zhang, X., 1993. A vegetation-climate classification system for global change studies in China. Quaternary Sci. 13, 157–169.
Zhang, X., Friedl, M.A., Schaaf, C.B., Strahler, A.H., Hodges, J.C.F., Gao, F., Reed, B.C., Huete, A., 2003. Monitoring vegetation phenology using MODIS. Remote Sens. Environ. 84, 471–475.
Zhang, G., Zhang, Y., Dong, J., Xiao, X., 2013. Green-up dates in the Tibetan plateau have continuously advanced from 1982 to 2011. Proc. Natl. Acad. Sci. U. S. A. 110, 4309–4314.
Zhang, Y., Xiao, X., Jin, C., Dong, J., Zhou, S., Wagle, P., Joiner, J., Guanter, L., Zhang, Y., Zhang, G., Qin, Y., Wang, J., Moore, B., 2016. Consistency between sun-induced chlorophyll fluorescence and gross primary production of vegetation in North America. Remote Sens. Environ. 183, 154–169.
Zhang, W., Zhou, T., Zhang, L., 2017a. Wetting and greening Tibetan plateau in early summer in recent decades. J. Geophys. Res.-Atmos. 122, 5808–5822.
Zhang, Y., Xiao, X., Wu, X., Zhou, S., Zhang, G., Qin, Y., Dong, J., 2017b. A global moderate resolution dataset of gross primary production of vegetation for 2000-2016. Sci Data 4, 170165.
Zhang, Q., Yao, T., Huemmrich, K.F., Middleton, E.M., Lyapustin, A., Wang, Y., 2020a. Evaluating impacts of snow, surface water, soil and vegetation on empirical vegetation and snow indices for the Utqiaġvik tundra ecosystem in Alaska with the LVS3 model. Remote Sens. Environ. 240.
Zhang, Y., Commane, R., Zhou, S., Williams, A.P., Gentine, P., 2020b. Light limitation regulates the response of autumn terrestrial carbon uptake to warming. Nat. Clim. Chang. 10, 739–743.
Zhang, Y., Parazoo, N.C., Williams, A.P., Zhou, S., Gentine, P., 2020c. Large and projected strengthening moisture limitation on end-of-season photosynthesis. Proc. Natl. Acad. Sci. U. S. A. 117, 9216–9222.